



The Emirates Mars Ultraviolet Spectrometer (EMUS) for the EMM Mission

Gregory M. Holsclaw¹  · Justin Deighan¹ · Hessa Almatroushi² · Mike Chaffin¹ · John Correia³ · J. Scott Evans³ · Matthew Fillingim⁴ · Alan Hoskins¹ · Sonal K. Jain¹ · Robert Lillis⁴ · Fatma Hussain Lootah² · Jason B. McPhate⁴ · Oswald H.W. Siegmund⁴ · Regina Soufli⁵ · Kush Tyagi¹

Received: 19 November 2020 / Accepted: 2 October 2021 / Published online: 26 October 2021
© The Author(s) 2021

Abstract

The Emirates Mars Mission (EMM) Hope probe was launched on 20 July 2020 at 01:58 GST (Gulf Standard Time) and entered orbit around Mars on 9 Feb 2021 at 19:42 GST. The high-altitude orbit (19,970 km periaapse, 42,650 km apoapse altitude, 25° inclination) with a 54.5 hour period enables a unique, synoptic, and nearly-continuous monitor of the Mars global climate. The Emirates Mars Ultraviolet Spectrometer (EMUS), one of three remote sensing instruments carried by Hope, is an imaging ultraviolet spectrograph, designed to investigate how conditions throughout the Mars atmosphere affect rates of atmospheric escape, and how key constituents in the exosphere behave temporally and spatially. EMUS will target two broad regions of the Mars upper atmosphere: 1) the thermosphere (100–200 km altitude), observing UV dayglow emissions from hydrogen (102.6, 121.6 nm), oxygen (130.4, 135.6 nm), and carbon monoxide (140–170 nm) and 2) the exosphere (above 200 km altitude), observing bound and escaping hydrogen (121.6 nm) and oxygen (130.4 nm).

EMUS achieves high sensitivity across a wavelength range of 100–170 nm in a single optical channel by employing “area-division” or “split” coatings of silicon carbide (SiC) and aluminum magnesium fluoride (Al+MgF₂) on each of its two optical elements. The EMUS detector consists of an open-face (windowless) microchannel plate (MCP) stack with a cesium iodide (CsI) photocathode and a photon-counting, cross-delay line (XDL) anode that enables spectral-spatial imaging. A single spherical telescope mirror with a 150 mm focal length provides a 10.75° field of view along two science entrance slits, selectable with a rotational mechanism. The high and low resolution (HR, LR) slits have angular widths of 0.18° and 0.25° and spectral widths of 1.3 nm and 1.8 nm, respectively. The spectrograph uses a Rowland circle design, with a toroidally-figured diffraction grating with a laminar groove profile and a ruling density of 936 gr mm⁻¹ providing a reciprocal linear dispersion of 2.65 nm mm⁻¹. The total instrument mass is 22.3 kg, and the orbit-average power is less than 15 W.

Keywords Mars · Atmosphere · EMM · Hope · Spectrograph · Ultraviolet

The Emirates Mars Mission
Edited by Dave Brain and Sarah Yousef Al Amiri

Extended author information available on the last page of the article

1 Introduction

The EMM mission uses a payload of complementary remote sensing instruments and a unique orbit to provide a global perspective of Martian atmospheric dynamics extending from the surface all the way to the edge of space. Extensive coverage will be obtained on both diurnal and seasonal timescales with a nominal mission duration of one Mars year. A comprehensive mission overview is provided in Amiri et al. (2021) and a synthesis of how the instruments' observations will be used to achieve science closure is provided in Al-Matroushi et al. (2021), both in this same issue. Here we list the highest level mission goals and focus in later sections on how the Emirates Mars Ultraviolet Spectrometer (EMUS) will contribute to them. The mission is based on three motivating science questions, with three associated objectives:

- I. How does the Martian lower atmosphere respond globally, diurnally and seasonally to solar forcing?

Objective A: Characterize the state of the Martian lower atmosphere on global scales and its geographic, diurnal and seasonal variability.

- II. How do conditions throughout the Martian atmosphere affect rates of atmospheric escape?

Objective B: Correlate rates of thermal and photochemical atmospheric escape with conditions in the collisional Martian atmosphere.

- III. How do key constituents in the Martian exosphere behave temporally and spatially?

Objective C: Characterize the spatial structure and variability of key constituents in the Martian exosphere.

In order to address these three objectives, four distinct investigations have been defined, each focused on a specific aspect and region of the Martian atmosphere:

1. Determine the three-dimensional thermal state of the lower atmosphere and its diurnal variability on sub-seasonal timescales.
2. Determine the geographic and diurnal distribution of key constituents in the lower atmosphere on sub-seasonal timescales.
3. Determine the abundance and spatial variability of key neutral species in the thermosphere on sub-seasonal timescales.
4. Determine the three-dimensional structure and variability of key species in the exosphere and their variability on sub-seasonal timescales.

The EMUS instrument contributes to investigations 3 and 4 by collecting remote sensing observations of UV photons emitted by the atoms and molecules that populate the tenuous Martian upper atmosphere. The structure of these investigations reflects the conventional division of a planetary upper atmosphere into the thermosphere (~100-200 km) where the atmosphere is collisional and temperature increases with altitude, and the exosphere (\gtrsim 200 km) where atoms and molecules travel on ballistic trajectories that can extend to great distances from the planet. For the purposes of studying the Martian exosphere in particular, we have defined inner, middle, and outer sub-regions that are based on the dominant physical processes (Fig. 1). Details of the major upper atmospheric processes and associated diagnostic UV emissions are described in the following section.

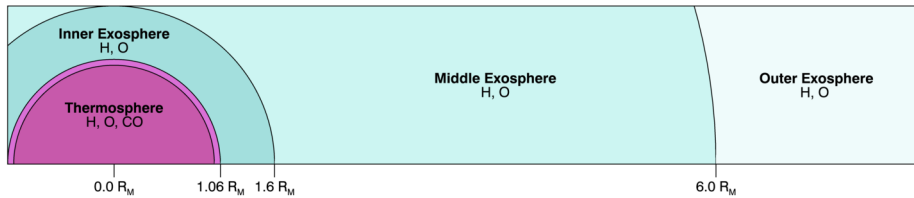


Fig. 1 EMUS science regions and target species for observation. The thermosphere consists of a mixture of collisional gases, experiences solar EUV energy deposition, and represents the source of atoms for the collisionless exosphere. The inner exosphere is tightly gravitationally bound and retains strong signatures of local density and temperature variations. In the middle exosphere the bound population declines with altitude and local variations become blurred. In the outer exosphere all atoms approach or exceed the escape velocity

2 EMUS Science Goals

2.1 Investigation 3: Thermosphere (100–200 km)

The thermosphere is a region characterized by intense heating by solar Extreme Ultraviolet (EUV) and X-ray radiation. This radiation drives energetic processes such as dissociation, ionization, and electronic excitation. A fraction of this energy is re-emitted as airglow at UV wavelengths, conveying information about the upper atmospheric structure and composition (Barth et al. 1967, 1971; Leblanc et al. 2006; Jain et al. 2015). There is substantial vertical transport of photochemically active species produced by dissociation, with H bearing species such as H_2O and H_2 being delivered upward from the lower atmosphere and CO_2 dissociation products O and CO being delivered downward to the lower atmosphere where they can recombine efficiently. Ionospheric photochemistry occurring within this domain is capable of producing non-thermal energetic neutrals which can be transported up even higher to the exosphere and, if sufficiently energetic, escape to space (Nagy et al. 1990). In addition, this region contains the homopause, where the atmosphere transitions from vertical transport dominated by turbulence (the homosphere) to molecular diffusion (the heterosphere), allowing species to stratify vertically by mass. The details of the atmospheric structure and rates of these processes vary substantially across the planet because the thermosphere is a highly dynamic region. The strong dayside solar EUV heating sets up a global diurnal circulation pattern (Stone et al. 2018). Gravity waves generated in the lower atmosphere grow in amplitude as they propagate into the upper atmosphere, resulting in significant modulations of composition and temperature (González-Galindo et al. 2015; Bougher et al. 2015a).

By characterizing the composition and spatial structure of the thermosphere, EMUS observations will provide insight into the processes that energize the upper atmosphere, track the coupling between the lower and upper atmosphere, and provide context for the lower boundary conditions of the exosphere. The fundamental measurements will be observations of UV dayglow emissions from H, O, and CO. These are the primary dissociation products of H_2O and CO_2 in the upper atmosphere, and have bright and well-defined emission features. See Fig. 2 for a simulated Mars Far Ultraviolet (FUV) spectrum with emission features identified. For details on how information about the atmosphere will be retrieved from the emission features see §4.

2.2 Investigation 4: Exosphere (Above 200 km)

The exosphere is defined as the low-density region of a planetary atmosphere where collisions between atoms and molecules are infrequent and their trajectories are predominantly

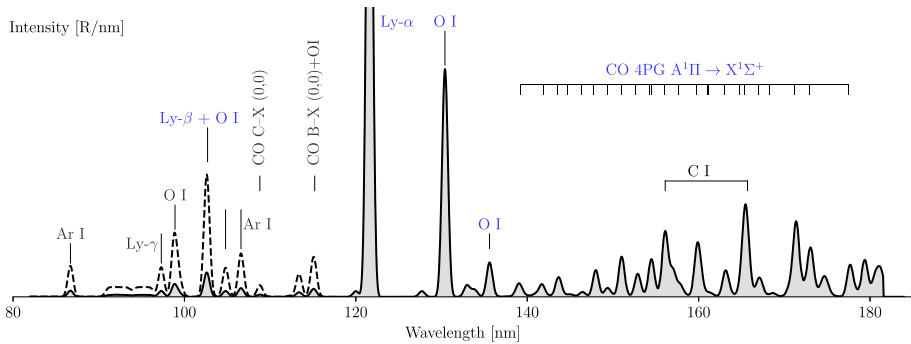


Fig. 2 Simulated spectrum for the extreme and far ultraviolet wavelength region corresponding to EMUS observations. The emissions features with blue legends, namely CO 4PG, O I 130.4 and 135.6 nm, and H I 121.6 nm (Ly- α) and 102.6 nm (Ly- β) will be used in the scientific retrieval (see Table 2). The EUV features below 118 nm (dashed line) have been scaled up by a factor of 10 for better visualization

ballistic (Johnson et al. 2008). The transition from the thermosphere to the exosphere, known as the exobase, occurs where the mean free path of the gas is equal to the density scale height, which at Mars is at approximately 200 km altitude or 1.06 R_M (Mars radii). With no collisions to inhibit them, low mass and/or high energy atoms are free to travel as high in the Martian gravity-well as their energy allows, even escaping the system entirely. By volume, the exosphere is mostly populated by atomic H due to its low mass (Anderson and Hord 1971; Chaufray et al. 2008; Lillis et al. 2015; Chaffin et al. 2015), as well as non-thermal or “hot” atomic O produced primarily by dissociative recombination of O_2^+ in the ionosphere (McElroy and McConnell 1971; Wallis 1978; Feldman et al. 2011; Deighan et al. 2015). These species form a diffuse corona of both gravitationally bound and escaping gas that extends to great distances from the planet.

The EMM mission concept sub-divides the exosphere into three parts, as shown in Fig. 1: (1) an “inner” region extending from 1.06 R_M to 1.6 R_M where the corona is populated primarily by lower energy atoms that are strongly gravitationally bound and remains highly coupled to spatial variations in the exobase source region, (2) a “middle” region extending from 1.6 R_M to 6.0 R_M where the fraction of atoms that are gravitationally bound declines with altitude and the effects of local variations across the planet become blurred, and (3) an “upper” region extending above 6.0 R_M which is populated by atoms with energies that approach or exceed the escape velocity. To characterize the global Martian exosphere, EMUS will measure variations in latitude, local time, and altitude by observing the solar resonant fluorescence of H and O in these three regions. This will provide a basis for understanding how the thermosphere and exosphere are coupled, as well as the rate at which H and O are being lost to space throughout the Martian year.

2.3 Prior UV Studies of the Martian Atmosphere and Advances

There is a rich history of studying the Martian atmosphere at UV wavelengths using space-based platforms. The first UV observations were made during fly-bys of the Mariner 6 and 7 spacecraft (Barth et al. 1967, 1969), followed by the orbiting Mariner 9 spacecraft (Stewart 1972). The Mariners 6, 7, and 9 ultraviolet spectrometers covered a range of 120–400 nm. Mariner 6 and 7 instruments measured the dayglow spectra in the wavelength range 110–210 nm with 1 nm resolution and from 190 to 430 nm with 2 nm resolution

Table 1 Major dayglow emission features observed on Mars

Species	Transition	Band System (Wavelength)	Major production mechanism
Ar I	3d → 3p	86.7 nm	RS(Ar)
	4s → 3p	104.8 nm	RS(Ar), EE(Ar)
	4s → 3p	106.7 nm	RS(Ar), EE(Ar)
C I	3d → 3p	127.7 nm	ED(CO ₂)
	4s → 3p	132.9 nm	ED(CO ₂)
	3D → 3P	156.1 nm	ED(CO ₂), RS(C)
	3P → 3p	165.7 nm	ED(CO ₂), RS(C)
CO	A ¹ Π → X ¹ Σ ⁺	Fourth Positive Bands (120.0–280.0 nm)	EE(CO), ED(CO ₂), RS(CO) PD(CO ₂), DR(CO ₂ ⁺)
	C ¹ Σ ⁺ → X ¹ Σ ⁺	Hopfield Birge bands ((0,0) at 108.8 nm)	RS(CO), ED(CO ₂)
	B ¹ Σ ⁺ → X ¹ Σ ⁺	Hopfield Birge bands ((0,0) at 115.2 nm)	RS(CO)
N ₂	A ³ Σ _u ⁺ → X ¹ Σ _g ⁺	Vegard-Kaplan 150.0–650.0 nm	EE(N ₂)
	a ¹ Π _g → X ¹ Σ _g ⁺	Lyman-Hopfield-Birge (120.0–260.0 nm)	EE(N ₂)
H	2p → 1s	Lyman-α (121.6 nm)	RS(H)
	3p → 1s	Lyman-β (102.6 nm) ^a	RS(H)
	4p → 1s	Lyman-γ (97.2 nm) ^a	RS(H)
O I	3S → 3P	130.2, 130.4, 130.6 nm	RS(O)
	5S → 3P	135.6, 135.8 nm	EE(O), ED(CO ₂)
	3P → 3D ⁰	98.9 nm	RS(O)
	3P ⁰ → 3S ⁰	104.0 nm	RS(O)
	1D → 1D ⁰	115.2 nm	RS(O)
N I	2P → 2D	149.3 nm	EI(N ₂)
O II	4S → 4P	83.4 nm	EI(O)
C II	2D → 2D ⁰	133.6 nm	EI(CO ₂), PI(CO ₂)

^aIncludes blended CO B–X (0-0) emission. RS: Resonance and Fluorescent Scattering; PI: Photoionization excitation; EI: photoelectron impact ionization excitation; EE: photo-electron impact; PD: Photodissociative excitation; ED: photo-electron dissociative excitation; DR: Dissociative recombination

(Pearce et al. 1971). Mariner 9 ultraviolet spectrometer (which was similar to that flown on Mariner 6 and 7) recorded the Martian dayglow spectra between 110 and 350 nm at 1.5 nm resolution for 120 days. The emission features observed by Mariner 6, 7, and 9 were: H I Lyman-α at 121.6 nm, O I 130.4 and 135.6 nm, C I 156.1 and 165.7 nm, the fourth positive (A¹Π – X¹Σ⁺) and Cameron bands (A³Π – X¹Σ⁺) of CO, and ultraviolet doublet (B²Σ⁺ – X²Π) and Fox-Duffendack-Barker (A²Π – X²Π) bands of CO₂⁺ (Stewart 1972; Barth et al. 1972). Soviet orbiters Mars 2 and 3 measured H I 121.6 nm and O I 130.4 nm

emissions between 1971 and 1972 (Dementyeva et al. 1972). After the Mariner and Mars series of spacecraft, the next set of airglow observations are carried out more than three decades later by Mars Express (MEx), the first planetary mission attempted by the European Space Agency (ESA). MEx carried a dedicated instrument for airglow measurements called Spectroscopy for the Investigation of the Characteristics of the Atmosphere of Mars (SPICAM) (Bertaux et al. 2006), which has broadened our understanding of dayglow phenomena. Dayglow emissions observed by SPICAM at UV wavelengths were similar to that observed by Mariner earlier (Bertaux et al. 2006; Leblanc et al. 2006; Shematovich et al. 2008; Simon et al. 2009; Cox et al. 2010; Gronoff et al. 2012), but with better sensitivity, and spatial and temporal coverage. Other observations of UV Martian airglow include that from the UV spectrograph Alice on the Rosetta spacecraft during a flyby maneuver (Feldman et al. 2011), and from Earth orbit by the Extreme UV Explorer (Krasnopolsky 2002), the Hubble Space Telescope (Paxton and Anderson 1992; Bhattacharyya et al. 2017), the Hopkins Ultraviolet Telescope (Feldman et al. 2000), and the Far UV Spectroscopic Explorer (Feldman et al. 2002).

More recent observations of the Martian atmosphere in the UV have been obtained by the Imaging UltraViolet Spectrograph (IUVS) onboard the MAVEN spacecraft and the Nadir and Occultation for MArS Discovery (NOMAD) instrument onboard the EXOMARS Trace Gas Orbiter. IUVS has provided long-term observations of the Martian thermosphere and exosphere that have helped characterize the structure, dynamics and energetics of the atmosphere (Jain et al. 2015; Deighan et al. 2015; Chaffin et al. 2018; Jain et al. 2020; Schneider et al. 2020). NOMAD has obtained UV solar occultation measurements of the lower and middle atmosphere and lower thermosphere, providing important constraints on ozone, dust opacity, and minor trace gases on Mars (Patel et al. 2017; López-Valverde et al. 2018).

These previous measurements have characterized the fundamental UV signatures in the Martian atmosphere, and provide a solid foundation of understanding upon which EMUS measurements will build. One of the primary limitations of orbiting Mars missions prior to EMM has been restrictions on spatial and temporal coverage, with variations being driven primarily by gradual precession of the spacecraft orbit over multiple months. In contrast, the EMM science orbit (19,970 km periapse, 42,650 km apoapse, 25° inclination) has been designed such that the instrument payload will be able to collect nearly complete global maps with full local time coverage every 9–10 days (Amiri et al. 2021; AlMatroushi et al. 2021). The high altitude science orbit also allows the EMUS instrument to observe out to extended altitudes in the middle and outer exosphere without the complications of being deeply embedded within the medium, as is the case for MEx/SPICAM and MAVEN/IUVS. In addition to this unprecedented coverage, EMUS is the first Mars orbiting spectrometer designed to be sensitive to extreme ultraviolet (EUV) wavelengths (<121 nm). See Fig. 2 for a spectrum of the various extreme and far ultraviolet emissions observed on Mars and Table 1 for detailed information about the associated electronic transitions and their excitation mechanisms.

3 Measurement Requirements

A flowdown of the physical quantities to be measured, observable UV emissions, and the necessary instrument requirements for EMUS to address Investigations 3 and 4 are provided in Table 2. This section describes the motivations for the values represented in that table. The column abundances of O and CO in the thermosphere will be derived from measurements of O I 135.6 nm atomic emission and CO 4PG band system respectively, while the abundance of H and O in the exosphere will be derived from measurements of H I 121.6 nm

Table 2 Flowdown of observables to measurement requirements. For details of the Observation Scenarios, see Fig. 3

Science Physical Quantity	Observable Emissions	Instrument Requirements		SNR-per Spatial Element	Observation Scenarios
		Spectral Resolution	Spatial Resolution		
Investigation 3: Thermosphere					
O Column Density	O I 135.6 nm	≤2.5 nm, 128-140 nm	≤300 km, 0.00-1.06 R _M	135.6 nm, 10 R: ≥5	U-OS1, U-OS2
CO Column Density	CO 4PG Band System	≤1.5 nm, 140-170 nm	≤300 km, 0.00-1.06 R _M	143.0 nm, 20 R: ≥3 146.0 nm, 20 R: ≥3 158.0 nm, 20 R: ≥3 159.7 nm, 20 R: ≥4 163.0 nm, 20 R: ≥3	U-OS1
Investigation 4: Exosphere					
H Density	H I 102.6 nm H I 121.6 nm	≤1.8 nm, 100-110 nm ≤5.0 nm, 110-130 nm	≤300 km, 1.06-1.60 R _M	102.6 nm, 10 R: ≥3 121.6 nm, 1000 R: ≥10	U-OS2, U-OS3, U-OS4
O Density	O I 130.4 nm	≤2.5 nm, 128-140 nm	≤1000 km, 1.60-6.00 R _M	102.6 nm, 1 R: ≥3 121.6 nm, 500 R: ≥10	U-OS3, U-OS4
			≤4000 km, 6.00-10.0 R _M	121.6 nm, 250 R: ≥10	U-OS3
			≤300 km, 1.06-1.60 R _M	130.4 nm, 30 R: ≥10	U-OS2, U-OS4
			≤1000 km, 1.60-6.00 R _M	130.4 nm, 0.1 R: ≥3	U-OS4

Within each investigation, a physical parameter retrieval accuracy of ≤30% (between species) and relative radiometric calibration ≤20% (between emission features) is required

(Lyman- α), H I 102.6 nm (Lyman- β), and O I 130.4 emission lines. These target emission features are identified with blue labels in the synthetic Martian spectrum shown in Fig. 2. In order to reliably measure the brightness of each target emission feature, it is necessary to spectrally resolve each one from other emission features at adjacent wavelengths. The driving requirement for the spectral resolution was found to be the ≤ 1.5 nm necessary to separate vibrational transitions within the CO 4PG molecular band system that are diagnostic of different excitation sources.

Spatial sampling of the thermosphere is required to be ≤ 300 km in order to be able to compare the observations with the output of existing global circulation models (GCMs) that include the upper atmosphere. These models typically have an output grid with at least 5° resolution in latitude and longitude, which corresponds to ~ 300 km in the tropics (Bougher et al. 2015b; González-Galindo et al. 2015). Spatial sampling in the exosphere is driven by the need to resolve its radial structure. In the inner exosphere ($1.06 R_M - 1.6 R_M$) a sampling of ≤ 300 km is required to resolve the scale height of thermal H and distinguish the vertical transition from a thermal O to non-thermal O dominated population. In the middle exosphere ($1.6 R_M - 6.0 R_M$) a more relaxed sampling of ≤ 1000 km is required, as the barometric formula begins to break down for thermal H (Chamberlain 1963) and the O population is entirely non-thermal. Finally, in the outer exosphere ($\geq 6.0 R_M$) a sampling of ≤ 4000 km is required, as both H and O densities have a nearly $1/r^2$ radial dependence due to approximate flux conservation as the atoms travel mostly radially at speeds approaching the escape velocity.

In order to track significant variations in the atmosphere it is necessary to have sufficient signal-to-noise (SNR) for the brightnesses measured in each of the spatial elements described above. Typical or average brightnesses for all target emission features are known from previous observations of Mars at EUV and FUV wavelengths (§2.3). The target air-glow emissions from the thermosphere are relatively bright since that is where most of the solar EUV energy is deposited. It was determined that the driving requirement for instrument sensitivity was obtaining adequate SNR for the faint H I 102.6 nm and O I 130.4 nm emissions from the tenuous exosphere.

For both investigations 3 (thermosphere) and 4 (exosphere) spatial coverage requirements are defined in terms of “standard image sets”, which must cover a certain range of geophysical conditions and be acquired within a certain timeframe and at certain temporal cadence. We first describe the standard image set spatial requirements for each investigation, and then the temporal requirements.

Since only one hemisphere of the planet can be observed at a given time, it is necessary to observe from multiple points of view around the orbit to achieve the objectives of characterizing the diurnal variations in the thermosphere and exosphere. The Mars-centered Solar Orbital (MSO) coordinate frame provides a convenient geometric frame for evaluating the atmospheric phenomena of interest. This orthogonal, right-handed frame is defined by the +X axis directed from Mars to the Sun, and the +Y axis pointing approximately opposite to that of the Mars orbit velocity vector. The +Z axis of the right-hand frame is parallel to the Mars orbit plane normal. Coverage requirements for operations can then be quantified by the MSO longitude (i.e. local time) of the spacecraft when it acquires an observation of Mars.

For investigation 3, the observational target is the portion of the disk illuminated on the dayside of the planet. Latitude illumination varies with season due to Mars’ obliquity of 25.2° , but the equatorial region within $\pm 20^\circ$ is always guaranteed to be well illuminated at a broad range of local times. In a standard image set this region is to be sampled in at least 6 of the 8 30° -wide intervals and at least 12 of the 16 15° -wide intervals in MSO

longitude spanning -120 to 120° (4 AM to 8 PM in MSO local time), respectively. This ensures complete coverage of the equatorial disk in MSO coordinates at emissions angles $\leq 70^\circ$, which avoids complications in analysis due to radiative transfer effects near the edge of the disk.

For investigation 4, the observational target is to sample the extended exosphere as seen from multiple view points around the orbit and at a range of altitudes throughout the inner, middle, and outer exosphere. The exosphere can be illuminated even in the night hemisphere at altitudes high enough to fall outside of the planet's shadow. And multiple scattering within the exosphere for an optically thick emission like H I 121.6 nm can illuminate the lower exosphere even within the shadow near local midnight (Chaffin et al. 2015). Images of H I 102.6 nm, H I 121.6 nm, and O I 103.4 nm in the inner exosphere region ($1.06 R_M - 1.6 R_M$) are required from at least 5 of the 8 45° intervals of MSO longitude spanning -180 to 180° , with no more than one 45° interval missed out of either the midnight-centered 90° -wide quadrant of 135 to -135° (to characterize the nightside hydrogen exosphere) or the three dayside-and-terminator quadrants spanning -135 to 135° (to characterize the dayside hydrogen and oxygen exosphere). These 2D images from around the orbit will enable 3D reconstruction of the neutral density distribution in the highly structured inner exosphere, a process known as tomography. Images of H I 121.6 nm in the less structured middle and outer exosphere regions ($1.6 R_M - \geq 6.0 R_M$) are required from near the sub-solar point at an MSO longitude of 0° ($\pm 30^\circ$) and also over either the dawn or dusk terminator 90° away ($\pm 5^\circ$), with both observations centered on nadir. This will allow for characterization of global scale asymmetries in the region of the exosphere populated by more energetic atoms. Finally, radial profiles of H I 102.6 nm, H I 121.6 nm, and O I 103.4 nm spanning the inner, middle, and outer exosphere regions ($1.06 R_M - \geq 6.0 R_M$) are required on the day hemisphere of the planet with lines of sight that intersect the MSO X-Z plane. This will allow for the radial structure of the densest and brightest part of the exosphere to be examined in detail. We specify a spectral resolution requirement of 1.8 nm, half the separation between O I 98.8 nm and H I 102.6 nm.

These standard observation sets for investigations 3 and 4 must be obtained at a temporal cadence which resolves the most important global scale variations in the Martian upper atmosphere. At the time of the EMM mission definition, it was recognized from existing observations that temporally resolving variations driven by the 28-day solar rotational modulation of solar EUV would be critical for interpreting UV emissions from both the thermosphere and exosphere (Jain et al. 2015; Deighan et al. 2015). In addition, there was observational evidence that the exchange of volatile H-bearing species between the lower and upper atmosphere could evolve over time scales of weeks (Chaffin et al. 2014; Clarke et al. 2014), dramatically faster than previous paradigms predicted. This was interpreted as vertical transport of H_2O followed by photolysis with the support of photochemical modeling (Chaffin et al. 2018). Based on this information, standard image sets are required to be obtained at a cadence of 1 week for the dynamic thermosphere and inner exosphere, with each image set acquired within 1/3 of a week. For the middle and outer exosphere imaging this is relaxed to a cadence of 2 weeks to adequately track the influence of solar EUV on the higher energy atoms. Finally, the dayside radial profiles are required to have at least 50% of the full altitude range collected in any given 1 week time-span, with 100% coverage required over a month.

While most data will be acquired at these standard observation cadences, during the EMM mission definition it was recognized that when studying Mars it is prudent to expect the unexpected. To allow the characterization of any unexpected short-term, sub-week temporal variability in all Mars seasons, the concept of "high cadence data sets" was incorporated into the coverage requirements. These consist of 3 consecutive standard image

sets in the same week, and must be collected in at least 7 of the 8 45° intervals of Solar Longitudes (Ls) comprising a Martian year. This ensures the opportunity to fully characterize differences in short-term ~ 2 day scale variability at all seasons. The value of including this strategy has been validated by recent observations of the upper atmosphere from the MAVEN mission showing dramatic short-term variability of hydrogenated species in the ionosphere (Stone et al. 2020) and neutral hydrogen in the exosphere (Chaffin et al. 2021). These studies show that during the onset of a large scale dust storm there may be substantial evolution of the upper atmospheric composition on the timescale of days, though the impact on escape rates is still dominated by the longer term effects in the following weeks. The EMUS temporal coverage requirements ensure that the EMM mission will be able to make major advances in characterizing the evolution of such events.

4 Observing Strategy and Data Processing

4.1 Instrument Design Summary

A detailed presentation of the EMUS instrument design and development is located in §5, but we give a brief summary here to provide context for the concept of operations described below. EMUS is an imaging spectrograph with a nominal wavelength range of 100–170 nm and is equipped with a mechanism that allows one of four rectangular apertures (or “slits”) to be positioned at the telescope focal plane. All slit lengths are the same, providing a projected angular height (full-width at half maximum, FWHM) of 10.75° . The high resolution (HR) and low resolution (LR) slits are provided for routine science observations and have angular widths of 0.18° and 0.25° , and nominal spectral widths of 1.3 nm and 1.8 nm, respectively. The other two slits are included for opportunistic science. EMUS is a body-fixed instrument, and all pointing is accomplished with spacecraft maneuvers. Most observations of the Mars atmosphere are obtained by continuously reading out the detector while drifting the EMUS FOV in the cross-slit direction in a raster pattern such that multiple swaths are required to cover a given region of interest.

4.2 Observing Strategy

In order to satisfy the measurement requirements described in §3 a set of four observation scenarios have been designed. The flowdown from the science quantities to the observation scenarios for each investigation are shown in Table 2. Below we describe the details of each observation sequence, which are illustrated in Fig. 3. For more information about how these fit into the overall observation strategy for the EMM mission see Amiri et al. (2021).

U-OS1: This observation supports Investigation 3 by measuring the spatial variability of oxygen (O I 135.6 nm) and carbon monoxide (CO 4PG: 140–170 nm) emissions in the thermosphere. It produces raster-scanned images of the disk of Mars covering $0\text{--}1.06 R_M$ ($8.9^\circ\text{--}17.5^\circ$, based on spacecraft altitude) at a slew rate of $0.0168^\circ \text{ sec}^{-1}$, giving a scan duration of ~ 17.4 minutes at 19,970 km and ~ 8.9 minutes at 42,650 km. The 1.3 nm slit is selected in order to resolve the spectral details of the CO 4PG band system. An observation set will be captured 2 times per spacecraft orbit, viewing the morning and afternoon hemispheres respectively, on one orbit per week.

U-OS2: This observation supports Investigation 4 by measuring the three-dimensional structure and temporal variability of oxygen (O I 130.4 nm), and hydrogen (H I 102.6, H I 121.6 nm) in the inner exosphere. The implementation is the same as U-OS1 except

that the raster scan covers $0\text{--}1.6 R_M$ ($13.4^\circ\text{--}26.1^\circ$, based on spacecraft altitude) obtained at a slew rate of $0.02^\circ \text{ sec}^{-1}$, giving a scan duration of ~ 21.8 minutes at 19,970 km and ~ 11.2 minutes at 42,650 km. The 1.8 nm slit is selected in order to trade increased signal against decreased spatial and spectral resolution when measuring the fainter but spatially smooth and spectrally well-separated emissions in the exosphere. An observation set will be captured 6 times per spacecraft orbit, and one orbit per week.

U-OS3 (a&b): This observation supports Investigation 4 by measuring the three-dimensional structure and temporal variability of hydrogen (H I 121.6 nm) in the middle and outer exosphere. The spacecraft will slew across 100° in an asterisk pattern centered on the disk and performed in 4 swaths at a rate of $0.5^\circ \text{ sec}^{-1}$. This will cover tangent altitudes from 0 to at least $7 R_M$ when the spacecraft is located at apoapsis. The slit position will be at 1.8 nm, and it will take 3.3 minutes per swath to cover 100° at all altitudes. An observation set will be captured 4 times per spacecraft orbit, with 2 observing the planet looking toward nadir (U-OS3(a)) and 2 observing the interplanetary hydrogen background by looking anti-nadir away from the planet on the opposite side of the orbit (U-OS3(b)). This allows for the hydrogen from the Martian exosphere to be distinguished from the hydrogen that fills the solar system. Orbits with these observations are to be scheduled at a cadence of 2 weeks.

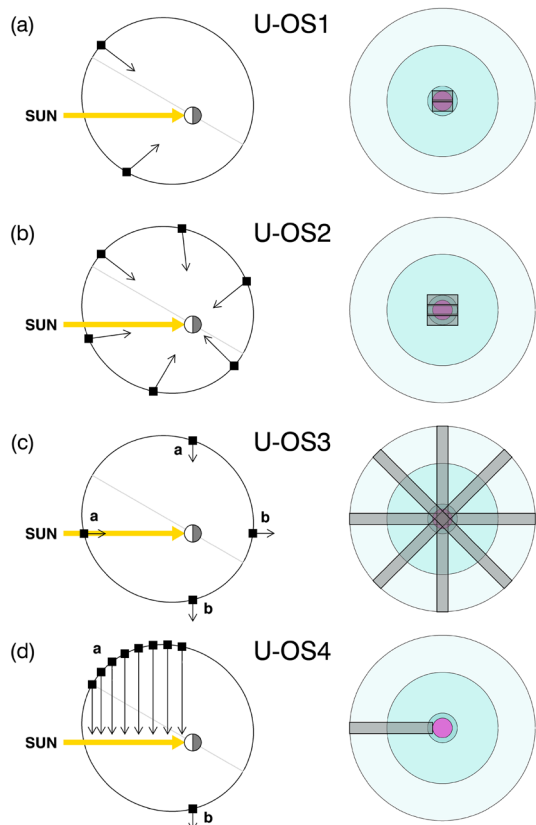
U-OS4 (a&b): This observation supports Investigation 4 by providing long exposure times for the mid and outer exosphere and will occur while the spacecraft is charging in a near-inertial orientation. There are two scenarios for this observation: 4a and 4b, as shown in Fig. 3. U-OS4(a) is a cross-exosphere observation with the instrument boresight vector in the plane of the spacecraft orbit, perpendicular to both the Mars-Sun line and orbit normal. EMUS will observe lines of sight in each 500 km altitude bin for tangent altitudes from $1.06 R_M$ to $\geq 6 R_M$ such that the boresight intersects the X-Z plane of the MSO coordinate system. The instrument slit position will be at 1.8 nm in order to obtain higher signal and it is planned to obtain full altitude coverage once per month. U-OS4(b) targets the interplanetary hydrogen background and points in the same direction (within 2°) of the U-OS4(a) that occurred on the opposite side of the orbit, such that the EMUS boresight does not intersect the X-Z plane of the MSO coordinate system. As with the U-OS3(b), the purpose of this measurement is to distinguish the hydrogen from the Martian exosphere from the hydrogen that fills the solar system.

4.3 Data Processing

4.3.1 L0 – L2a Pipeline: Packets to Calibrated Spectra

The packetized telemetry stream from the Hope spacecraft is received by the NASA Deep Space Network ground stations and relayed to the Mission Operations Center (MOC) at the Mohammed Bin Rashid Space Centre (MBRSC) in Dubai, United Arab Emirates (UAE). The MOC divides the packets into science and housekeeping for each instrument, and sends the resulting Level 0 data files to the Science Data Center (SDC), which operates on cloud resources provided by Amazon Web Services (AWS). New data triggers EMUS automated processing on an AWS Elastic Cloud Computing (EC2) instance using software provided by the EMUS Instrument Team Facility (ITF) at the University of Colorado Laboratory for Atmospheric and Space Physics (LASP). After packets are extracted from the L0 files and stored in a database, science data is retrieved to create Level 1 data products. Each EMUS observation, a sequence of images at a fixed instrument configuration (see §5.5.2), results in a single L1 data product that consists of raw detector images in units of counts and a set of ancillary data that has been converted from digitized values to physical units (e.g.

Fig. 3 EMUS Observation Scenarios. The diagrams on the left show the position of the spacecraft in its orbit (square symbols) and lines of sight (arrows) relative to Mars and the Sun for a complete set of observations. The diagrams on the right show each observation from the point of view of the spacecraft, with the area scanned by the 10.75° tall instrument airglow slit (grey rectangles) overlaid on the science regions of interest (see Fig. 1 for details)



temperature in degrees celsius). Level 2a products contain calibrated data in the quantity of spectral radiance, and there is a one-to-one correspondence with an L1 product. L2a products also contain a comprehensive set of geometry parameters, calculated using SPICE kernels provided by the MOC to the SDC. See the complete list of EMUS data products in Table 3.

4.3.2 L2a – L2b Pipeline: Derivation of Emission Feature Brightnesses

The extreme and far-ultraviolet region of the electromagnetic spectrum observed by EMUS is a rich blend of several atomic and molecular band emissions as shown in Fig. 2 and listed in Table 1. The major emission features in the FUV region are the CO fourth positive bands ($A^1\Pi \rightarrow X^1\Sigma^+$), H I 121.6 nm line, C I 156.1 and 165.7 nm lines, and O I 130.4 and 135.6 nm lines. The EUV spectrum consists mainly of emissions from atomic Ar I 86.7, 104.8, and 106.7 nm; O I 98.9, 104.0, and 115.2 nm; H I 97.2 and 102.6 nm; and the CO Hopfield-Birge molecular bands ($B^1\Sigma^+ \rightarrow X^1\Sigma^+$ and $C^1\Sigma^+ \rightarrow X^1\Sigma^+$) (Barth et al. 1967, 1971; Leblanc et al. 2006; Jain et al. 2015).

To extract the brightness of targeted emission features for the retrieval algorithm, we use a Multiple Linear Regression (MLR) routine to fit the observed spectrum for each spatial pixel using a similar approach to that employed by MAVEN/IUVS (Jain et al. 2015; Stevens et al. 2015). Model spectral templates in physical space (radiance) for each unique feature

Table 3 EMUS data products

Level	Description
0	Binary CCSDS packets from the spacecraft. Generated by the MOC, delivered to SDC. Divided into science and housekeeping files.
1	Detector images stacked in files according to instrument commanding with a consistent instrument configuration. The science image will remain uncalibrated data numbers, everything else will be in engineering units (e.g. °C for temperature).
2a	Detector images, in calibrated units, stacked in files according to instrument commanding, with added geometry and pointing information.
2b	Perform model fits of brightnesses on selected wavelengths or bands (H Ly α , Ly β , O 1304, O 1356, CO), with added geometry and pointing information.
L3 disk	Line-of-sight column density for O, CO above a reference pressure of 0.2 mPa
L3 H corona	Line-of-sight column density profile for H; Tangent point density profile; Escape Rate
L3 O corona	Line-of-sight column density profile for O; Tangent point density profile; Escape Rate

are run through a software instrument simulator that applies various instrumental effects to the spectra, including: the radiometric sensitivity, global dead time, mapping to the distorted wavelength scale, pixel binning, and convolution by the line spread function (LSF). The simulator output is an estimate of the instrument response in units of counts that can then be compared directly with a measurement. The MLR routine fits the template spectra to the data, and the following parameters are recorded in L2b data products: fit coefficients (template weights), composite fit spectrum in units of counts, and the derived brightness of each feature.

4.3.3 Level 3 Overview: Emission Line Brightness to Geophysical Quantities

For many scientific studies, it is useful to derive physical quantities such as species density and temperature from the reduced brightnesses contained in the L2b products. Due to the varying goals and optimal strategies for performing a retrieval for each species in each domain of the atmosphere, four distinct pipelines are employed for the production of Level 3 products. The results are collected into two types of Level 3 products: disk and corona. Observations that cover both the disk and corona, such as U-OS2, may be processed to have both types of Level 3 products.

4.3.4 O Disk

The thermospheric oxygen column density will be determined from measurements of the O I 135.6 nm emission. This emission feature on the Martian dayside is produced by oxygen atoms transitioning to their ground state after being excited into the 5S state by photoelectron impact on oxygen with a minor contribution from CO₂. Our primary tool is a forward model that accounts for eddy and molecular diffusion, temperature structure, photoelectron production, energy degradation, and excitation, as well as the attenuation of emitted 135.6 nm photons (Jain 2013). This model generates 135.6 nm brightnesses given the following inputs: solar EUV spectrum, emission angle, solar zenith angle, exosphere temperature, N₂ and Ar

mixing ratios (fixed with respect to each other at the ratio of 0.71) (Trainer et al. 2019) and eddy diffusion coefficient. For each U-OS1 and U-OS2 observation, the first three inputs are known: solar zenith angle (SZA) and emission angle from the observation geometry, and the solar EUV spectrum from the FISM-M model (Thiemann et al. 2017) (which takes inputs from solar EUV-measuring assets at Earth and Mars). The latter three inputs (exosphere temperature, mixing ratio, and eddy diffusion coefficient) are unknown and varied over reasonable expected parameter ranges (taken from data from MAVEN NGIMS (Mahaffy et al. 2015) and the Mars Climate Database of global atmosphere simulations (González-Galindo et al. 2015)) to construct a multidimensional lookup table. Each combination of these inputs corresponds to an altitude profile of neutral density and oxygen column density ratio above a reference pressure level (0.2 mPa) near the airglow peak. For each pixel, the retrieved oxygen column density is that associated with the best match from the lookup table to the EMUS-observed brightness. Uncertainty in the retrieved oxygen column density will be determined via propagation of known errors in the solar EUV spectrum and measured airglow brightnesses, and reasonable error estimates in N_2 and Ar mixing ratio. This retrieval will be described in detail in a forthcoming manuscript.

4.3.5 CO Disk

The $\Sigma CO/CO_2$ algorithm (where Σ indicates a quantity integrated along a line of sight) provides a measure of relative composition within the Martian thermosphere by deriving the column abundance of CO above a fixed reference column of CO_2 for U-OS1 observations. This algorithm traces its roots back to the $\Sigma O/N_2$ algorithm used at Earth for inferring relative composition from remote sensing observations (Strickland et al. 1995; Evans et al. 1995). The algorithm uses a lookup table approach by first generating a series of model atmospheres that span the expected range of physically realistic atmospheres. The AURIC model (Strickland et al. 1999; Evans et al. 2015) is then used to calculate column emission rates and spectral radiances as functions of CO/CO_2 column density ratio, solar zenith angle, and emission angle for the range of input model atmospheres. When used with EMUS observations, the lookup table provides a unique mapping from intensity ratio to CO/CO_2 column density ratio for a given solar zenith angle and emission angle. Intensities from selected bands (listed in Table 2) of the optically allowed fourth Positive Group (4PG) band system ($A^1\Pi \rightarrow X^1\Sigma^+$) of CO are used as signatures of CO and CO_2 .

4.3.6 H Corona

EMUS observes the hydrogen corona and thermosphere at H I 121.6 nm and H I 102.6 nm. These observations are used to constrain the density and temperature of H at the exobase. We retrieve 0th and 1st order spherical harmonic distributions of the exobase/upper thermosphere temperature, and a mean atmospheric density under the assumption that local densities are governed by the $n \cdot T^{5/2} = \text{constant}$ relationship of Hodges (Hodges and Johnson 1968). In addition to thermal H, we may also retrieve proton aurora brightness, deuterium densities, and hot H densities from their contribution to the H I 121.6 nm brightness on and near the disk, as well as thermospheric oxygen densities (from the O 102.6 nm emission blended with H I 102.6 nm), and interplanetary hydrogen brightnesses from background observations. The exact set of targeted retrieval parameters will be determined based on data quality and the level of modeling effort required. We will perform one retrieval per week (~ 3 orbits) of observations, including all planetary observation sets (U-OS1, U-OS2, U-OS3, and U-OS4). The retrieval algorithm ingests measured brightnesses and the solar

irradiance at H I 121.6 nm and H I 102.6 nm, and MSO look directions. Using these, it forward-models the optically thick scattering that produces these emissions for an assumed density and temperature distribution, iteratively updating the input parameters (and estimating their uncertainties) until the observations are well-reproduced.

4.3.7 O Corona

Measurements of the O I 130.4 nm triplet above 700 km will be used to retrieve the characteristics of atomic oxygen in the exosphere surrounding Mars. At these altitudes this emission is optically thin, stimulated solely by solar resonant fluorescence, and the atomic oxygen corona is populated exclusively by non-thermal processes in the thermosphere. Multiple observations will be integrated in each retrieval, relying primarily on U-OS2 and U-OS4 data collected within approximately one week (equivalent to ~ 3 orbits). The U-OS2 data will inform the 3D structure of the inner corona while the U-OS4 data will constrain the contributions of the gravitationally bound and escaping atomic oxygen populations. Retrievals will be performed through iterative forward modeling of exospheric densities and line-of-sight brightnesses. The forward modeling will incorporate global scale geographic variations in non-thermal oxygen production using a spherical harmonic framework, and the fitted coefficients for the orders and degrees considered will be reported. Exospheric asymmetries in solar zenith angle, local time, and latitude are expected to be readily constrained. In addition, retrieved line-of-sight densities will be reported, along with an estimate of the global escape rate of atomic oxygen.

5 Instrument Implementation

5.1 Overview

From the measurement requirements defined in §3 and Table 2 we derive and specify verifiable, functional requirements for the instrument in Table 4. The EMUS instrument has been designed using several heritage subsystems to meet these requirements with adequate margin, and consists of two components: 1) the “spectrograph”, which includes the optical channel, detector and its electronics, and high voltage power supply (HVPS) and 2) the electronics box, which includes three boards connected by a common backplane: power, channel control, and processor board with the FPGA. (The term “channel” is a vestige from its heritage implementation where two optical channels existed.) A block diagram of the EMUS subsystems is in Fig. 4 and an annotated diagram in Fig. 5.

5.2 Instrument Accommodation

The EMUS electronics box, Emirates Exploration Imager (EXI), Emirates Mars Infrared Spectrometer (EMIRS), and star trackers are mounted to the primary payload deck, whereas the EMUS spectrograph – seen in Fig. 6 – is attached to a subpanel with a normal vector parallel to the spacecraft +X axis. The relationship between the local EMUS coordinate frame and the spacecraft frame is illustrated in Fig. 7. After integration to the spacecraft, the angle between the EMUS boresight vector (EMUS frame +Z) and the spacecraft +Y axis was required to be no more than 20 arcmin; the measured value was ~ 5 arcmin. The long dimension of the EMUS entrance slits (+Y EMUS frame) is approximately parallel to the spacecraft X axis.

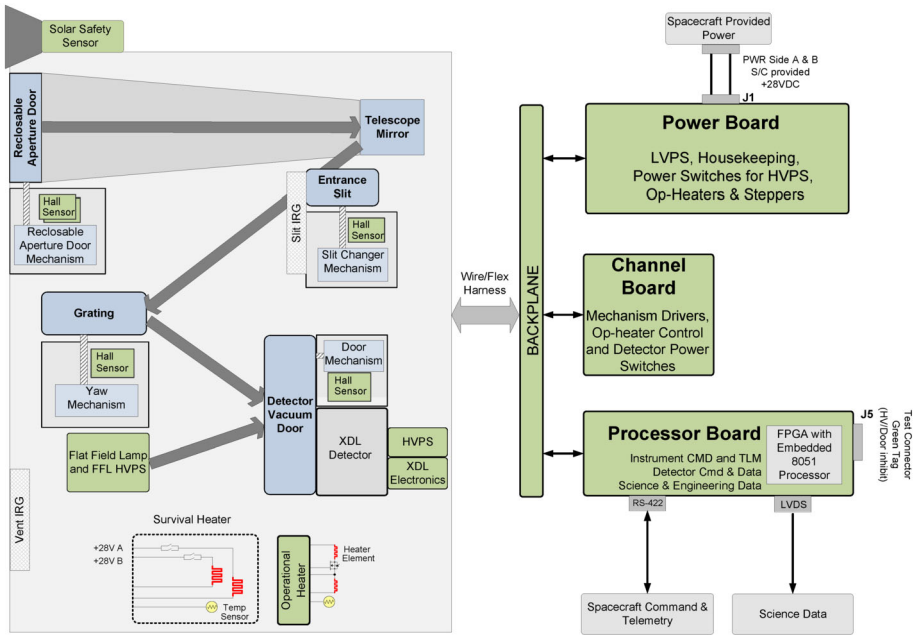


Fig. 4 EMUS functional block diagram

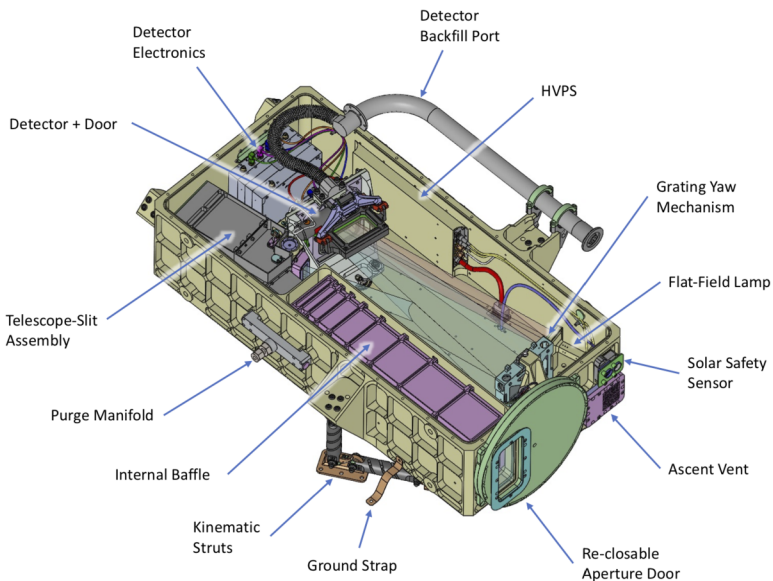
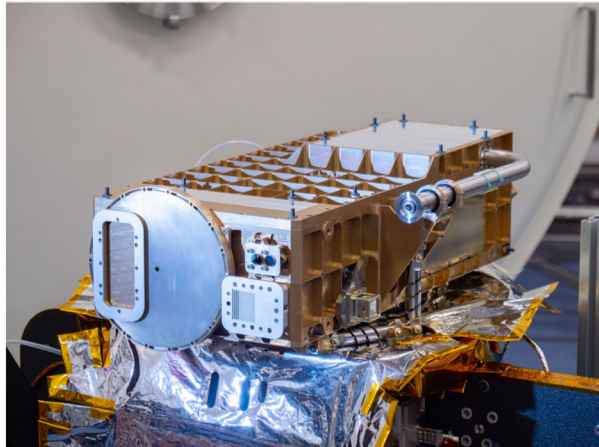


Fig. 5 EMUS major components and subsystems

The total mass of the EMUS instrument is 22.3 kg, with a component breakdown given in Table 5. Orbit average power is less than 15 W, and includes an estimated maximum of 6.6 W of proportional heater control.

Table 4 Instrument functional requirements

Parameter	Requirement	
Wavelength range	100–170 nm	
Spectral resolution	1.5 nm at 140–170 nm 1.8 nm at 100–130 nm	
Field of view	10.6°	
Spatial resolution	0.36°	
Sensitivity	wavelength (nm)	throughput (c/ph)
	102.6	3.91E-03
	121.6	4.75E-04
	121.6	4.75E-04
	135.6	5.25E-03
	143.0	4.78E-03
	146.0	4.78E-03
	158.0	3.19E-03
	159.7	5.25E-03
163.0	3.19E-03	

Fig. 6 The EMUS spectrograph is attached to a subpanel of the main instrument deck with 6 titanium struts arranged in 3 bipods

5.3 Optical Design and Predicted Performance

We employ an imaging spectrograph as the EMUS instrument optical design, drawing from elements of similar instruments, including: the Global-Scale Observations of the Limb and Disk Mission (GOLD) (McClintock et al. 2020; Siegmund et al. 2016), the Mars Atmosphere and Volatile Evolution (MAVEN) (Jakosky et al. 2015) Imaging UltraViolet Spectrograph (IUVS) (McClintock et al. 2015), and the Cassini Ultraviolet Imaging Spectrograph (UVIS) (Esposito et al. 2004). Typically, a minimum of two reflective surfaces is required (telescope, imaging diffraction grating) for an instrument of this type, and so EMUS shares this basic layout with Cassini UVIS. While additional optical surfaces could improve imaging performance, simplify packaging, or optimize instrument placement, the resulting loss

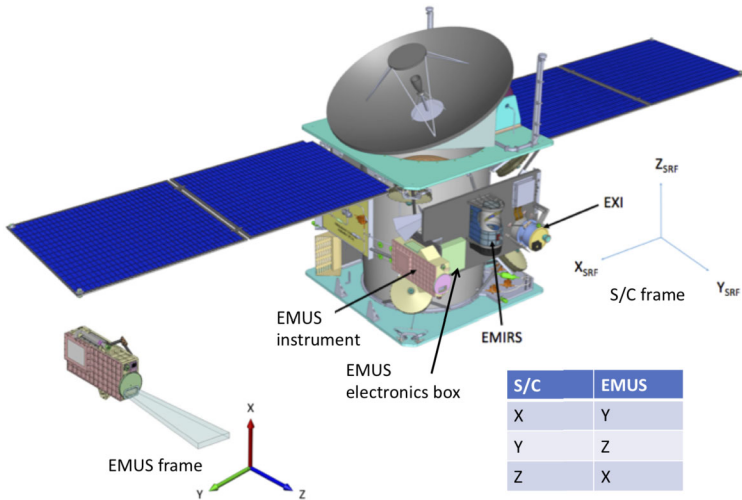


Fig. 7 The EMUS instrument frame is oriented such that the +Z direction (optical boresight) is parallel to the spacecraft +Y direction, while the instrument +Y direction is parallel to spacecraft +X

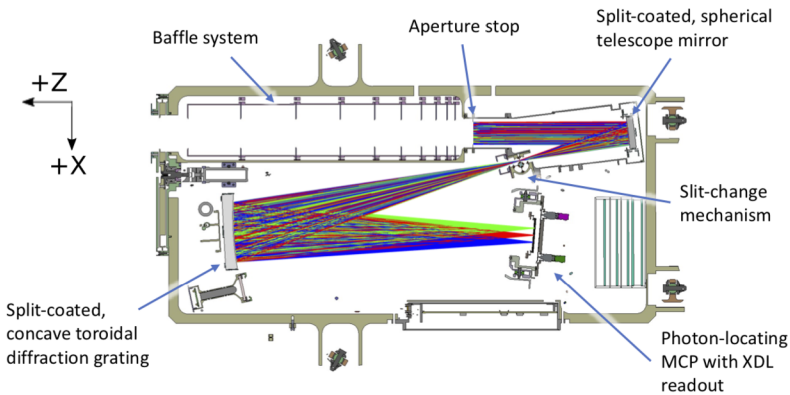


Fig. 8 The EMUS optical design is based on a Rowland circle spectrograph, using a concave toroidal imaging diffraction grating, fed by a single-element telescope mirror. A photon-locating, open-face MCP with a cesium iodide photocathode and cross delay line readout enables sensitivity in the spectral range 100–170 nm. The EMUS instrument frame is indicated

in throughput due to low surface reflectance – particularly at the required wavelength of H I 102.6 nm – would be significant and unacceptable. Sufficient throughput at this wavelength is provided by area-division optical coatings of silicon carbide (SiC) and aluminum with a magnesium fluoride overcoat ($\text{Al}+\text{MgF}_2$). Figure 8 shows the optical path in the dispersion plane.

5.3.1 Telescope

Here we discuss the components that make up the telescope, and consider them in the order that light propagates through the system: 1) the Reclosable Aperture Door (RAD), 2)

light baffle, 3) aperture stop (coincident with the entrance pupil), 4) spherical mirror, and 5) entrance slit.

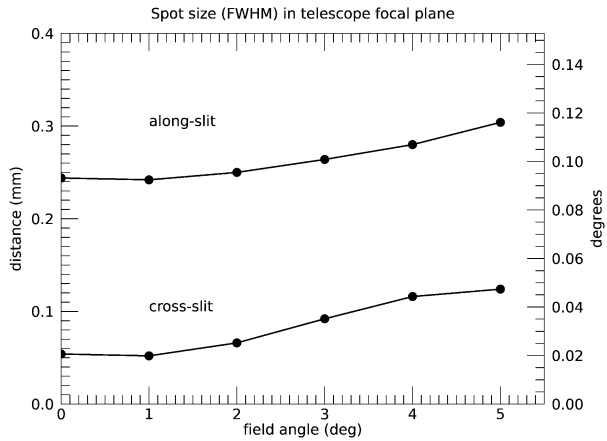
The RAD is located at the front end of the telescope baffle. This commandable, rotational door mechanism protects against the inadvertent pointing of the EMUS field of view (FOV) at the Sun and minimizes contamination during ground assembly, integration, and test (AI&T) activities. The RAD is opened only during active observations. See § 5.6.3 for more details.

A ~ 372 mm long telescope baffle controls scattered light from bright, out-of-field sources which include the Sun and Mars itself when viewing the considerably fainter exosphere. Vanes are positioned such that only the unilluminated backside is visible to any point within the aperture stop; therefore, a minimum of two scattering events must occur before light can enter the telescope cavity. All surfaces within the baffle are unpolished, conversion-coated aluminum. Vane depth on the inboard side (EMUS +X) is smaller than the others due to space constraints resulting from minimization of the telescope mirror opening angle; vane spacing is determined based on this constraint and symmetric on all sides (see Fig. 8). The full angles at which an out-of-field source can enter the aperture stop are $11.5 \times 18.4^\circ$ (spectral \times spatial), which we term the “degradation” boundary due to the potential for stray light to enter the entrance slit. The full angles at which an out-of-field source illuminates the edge of the telescope mirror are $7.9 \times 16.0^\circ$ (spectral \times spatial), which we term the “damage” boundary due to the potential for photo-polymerization of residual hydrocarbons on the optical surfaces by solar EUV and subsequent loss in throughput (BenMoussa et al. 2013).

The GOLD instrument (McClintock et al. 2020) telescope assembly was found to meet EMUS requirements, and was adopted with slight modifications. While increasing the FOV beyond what this heritage implementation provides would bring operations efficiency, such a design change would have also brought unwanted complexity. As specified in §3, the optical system must resolve atmospheric features 300 km in size; from a maximum spacecraft altitude of 44,000 km, this corresponds to an angle of 0.36° . A single spherical mirror with a focal length of 150 mm and opening angle of 14° provides sufficient imaging performance over the full field of 10.75° while allowing sufficient space for the slit-change mechanism. The aperture stop is located in front of the telescope mirror and defines the amount of light entering the system. The collimated beam from a hypothetical point source located at infinity, originating from any field angle, passes through and fills the aperture stop, and any conjugate image of the stop shares this property. We define the location of the EMUS aperture stop such that its conjugate image, created by the telescope mirror, forms at the diffraction grating, bringing two advantages: 1) the size of the grating is minimized, and 2) translation of the beam on the grating as a function of field angle is eliminated. This placement of the aperture stop is dependent on the spectrograph design, described below, and results in a telescope / aperture stop separation of 206 mm. The dimensions of the aperture stop, 30×20 mm (cross-slit \times along-slit or spectral \times spatial), are determined in the design process that is described in the next subsection.

The telescope imaging performance is determined by analyzing the resultant spot size (i.e. the point spread function or PSF) of incident collimated light raytraced using Zemax OpticStudio across the full range of field angles. Astigmatism is a dominant aberration in spherical surfaces used off axis, and so the distance between the telescope and spectrograph entrance slit is optimized such that the field-averaged, cross-slit image size is a minimum (i.e. at the tangential focus). The cross-slit width and along-slit height of images was found at six field positions and shown in Fig. 9. Using the full-width at half maximum (FWHM) metric for image size, we find that the image height increases with field angle from 0.25 mm

Fig. 9 Predicted EMUS telescope imaging performance as real-space image size (FWHM, units of mm, left axis) and projected angle (units of degrees, right axis) versus field angle in degrees. Due to astigmatism the images are asymmetric, and so the size is given in two perpendicular directions: cross-slit and along-slit



(0.09°) at 0.0° to 0.30 mm (0.12°) at 5.0°, while the image width increases from 0.05 mm (0.02°) at 0.0° field to 0.12 mm (0.05°) at 5.0° field. These results demonstrate that the heritage telescope can meet the 0.36° spatial resolution requirement.

The instrument FOV is defined by the projected angular size of the spectrograph entrance slit located in the telescope focal plane. Multiple slit positions are enabled by a heritage four-position rotational mechanism developed for use in the GOLD instrument (McClintock et al. 2020). To satisfy the spectral resolution requirements of Investigation 3 (1.5 nm) and Investigation 4 (1.8 nm) specified in §3, we define two science slit apertures to provide nominal spectral resolutions of 1.3 nm and 1.8 nm, respectively, resulting in linear widths of 0.48 mm and 0.67 mm (see derivation in the next subsection). Given the focal length of 150 mm, these slits correspond to projected angles of 0.18° and 0.25°. The two remaining slots in the mechanism are populated with apertures for opportunistic science with spectral resolutions of ~ 0.35 nm (over a restricted field angle range) and 5 nm, corresponding to respective linear widths of 0.12 mm and 1.85 mm, and projected angles of 0.046° and 0.71°. The long-slit dimension of each aperture is 28.9 mm. While this results in a paraxial FOV of 11°, the true FOV is less when considering the aberrated PSF and vignetting by the slit. Theoretically, the unvignetted FOV of the telescope system will be 10.75° with a FWHM FOV of 10.9° with the slit placed at the telescope focal plane (i.e. with a separation of 150 mm). Changing the mirror-slit separation to minimize the cross-slit PSF size and maximizing the cross-slit resolution has the side effect of slightly decreasing the FOV to a measured value of 10.75° FWHM.

The spatial resolution of the system is determined by the convolution of the telescope PSF with the entrance slit aperture in the cross-slit dimension, and the combined imaging properties of the telescope and spectrograph in the along-slit dimension. The widths of the two science slits are larger than the telescope PSF, and thus the cross-slit FOV is equivalent to the geometric values above. The along-slit spatial resolution is considered in the next subsection.

5.3.2 Spectrograph

The optimal configuration of a spectrometer with a single, reflective concave diffraction grating is known as the Rowland circle spectrograph (Rowland 1883). For a grating of spherical figure with radius R , a circle of *diameter* R exists in the dispersion plane, located such

Table 5 Instrument design summary

Entrance pupil	30×20 mm (spectral×spatial)
Telescope	
Focal length	150 mm
Figure	sphere, R=300 mm
Coating	half Cr+SiC, half Al+MgF ₂
Field of view	
High resolution slit	0.18×10.75°(0.48×28.9 mm)
Low resolution slit	0.25×10.75°(0.67×28.9 mm)
Imaging distance, slit-to-grating	392.6 mm
Imaging distance, grating-to-detector	398.7 mm
Diffraction grating	
Figure	toroid, $R_v=390.7$ mm, $R_h=400$ mm
Ruling density	936 grooves mm ⁻¹
Groove profile	laminar
Coating	half SiC, half Al+MgF ₂
Reciprocal linear dispersion	2.65 nm mm ⁻¹
Wavelength range ^a	
across full 10.75°	100-163 nm
center chord at 0°	83-180 nm
Spectral Resolution	
Very High Resolution (VHR)	0.4 nm (central 1°, 130–160 nm)
High Resolution (HR)	1.3 nm
Low Resolution (LR)	1.8 nm
Very Low Resolution (VLR)	5.0 nm
Detector	
Active area	38 mm diameter
Anode	cross delay line
Format ^b	1728×1536 (spectral×spatial)
Pixel size, average	22.8×26.4 μm (spectral×spatial)
Mass	
Spectrograph	18.0 kg
Ebox	3.2 kg
MLI	0.7 kg
Harnesses	0.4 kg
Power	< 15 W (orbit average)
Dimensions	
Spectrograph	73×50×22 cm
Ebox	24×25×10 cm

^anominal GYM position of 152 DN

^bslightly oversized of the circular active area

that the grating center and its center of curvature lie on the circle, and the normal of the surface defined by this circle is parallel to the rulings. This curve defines the locus of points where a source positioned on the circle is diffracted and imaged by the grating back to the circle at the optimal spectral (tangential) focus. The spatial (sagittal) focus exists on a line behind this curve, and so this basic configuration exhibits significant astigmatism. This aberration can be controlled by replacing the classic spherical figure of the grating with a toroid, as will be described.

The detector provides an unvignetted rectangular area of 26×28.9 mm onto which is mapped the spectral and spatial subtense of the instrument. For the required wavelength range of 100–170 nm, the theoretical reciprocal linear dispersion (RLD) is 2.69 nm mm⁻¹. We can determine the geometry of the spectrograph arrangement starting with the grating equation:

$$\sin \alpha + \sin \beta = N m \lambda \quad (1)$$

where α is the incidence angle, β is the diffraction angle, N is the ruling density, m is the order, and λ is the wavelength. Differentiating, with α constant (source fixed), leads to:

$$\cos \beta \, d\beta = N m \, d\lambda \quad (2)$$

Angle $d\beta$ is proportional to the linear width dl (oriented perpendicular to the diffracted ray) subtended by wavelength range $d\lambda$ and inversely proportional to the imaging distance to the detector, d_d :

$$d\beta = \frac{dl}{d_d} \quad (3)$$

The linear distance dx along the Rowland circle is larger than dl by $\cos \beta$ because it is tilted with respect to the diffracted ray. Substituting this relation into the previous equation and solving for N gives:

$$N = \frac{\cos^2 \beta}{d_d m \frac{d\lambda}{dx}} \quad (4)$$

As mentioned previously, a Rowland spectrograph (Rowland 1883) places the entrance slit and exit slit (in this case, the detector) on a circle of diameter R (the grating radius of curvature), leading to the distances:

$$\begin{aligned} d_e &= R \cos \alpha \\ d_d &= R \cos \beta \end{aligned} \quad (5)$$

where d_e is the distance from the entrance slit to the grating. Substituting the expression for d_d into the above ruling density equation gives:

$$N = \frac{\cos \beta}{R m \frac{d\lambda}{dx}} \quad (6)$$

Rays in the dispersion (horizontal) plane are brought to a focus at the Rowland circle, while rays in the spatial (vertical) plane are brought to a focus along a curve that is approximately linear and perpendicular to the grating normal. The position of the spatial focal curve

can be manipulated by choice of the radius of curvature (ROC) of the grating in the spatial dimension, thereby defining a toroidal figure. Decreasing the ROC in this dimension brings the spatial focal curve closer to the grating, and intersects the Rowland circle at up to two locations. The relationship between the ROC in the spatial plane (R_v), the spectral plane (R_h), and the diffraction angles (β , $-\beta$) at the stigmatic wavelengths is (Haber 1950; Huber and Tondello 1979):

$$\frac{R_v}{R_h} = \cos \alpha \cos \beta \quad (7)$$

Due to this symmetry about the grating normal, the preferred arrangement is to place the center of the detector at a diffraction angle of zero. However, space constraints between the detector assembly and slit-change mechanism limit the distance between the center of the detector active area and the entrance slit to ~ 100 mm. Off-axis imaging aberrations are proportional to the opening angle of the grating – the angle between the object (slit) and image (detector center) as seen from the grating – and thus longer instruments provide better performance. The imaging distance from the detector to the grating is limited to ≤ 400 mm by spacecraft mechanical constraints; we assume this distance, thereby setting R_h to be 400 mm. We assume a focal ratio of 5, defining the dimensions of the aperture stop to be 30×30 mm. We find through raytrace analysis that this design does not quite meet the driving spectral resolution requirement of 1.5 nm over the entire field. By reducing the entrance aperture size in the spatial dimension from 30 mm to 20 mm (i.e. increasing the focal ratio from 5 to 7.5) the spectral imaging properties improve so that the resolution requirement is comfortably met over the entire field at all wavelengths (see §5.3.3). With $d\lambda/dx=2.69$ nm mm^{-1} and $R_h=400$ mm, we find $N=926$ gr mm^{-1} , $d_e=392.6$ mm, $\alpha=11^\circ$, and $\beta=3.8^\circ$ at $\lambda=135$ nm. A higher ruling density of $N=936$ gr mm^{-1} was inadvertently communicated to the grating vendor, resulting in a slightly higher dispersion (lower RLD) of 2.67 nm mm^{-1} ; this has negligible impact on any imaging performance metric. The grating ROC in the spatial dimension (R_v) is allowed to vary in order to minimize the spot size along the same direction. The final design parameters are determined through raytracing optimization, and are found in Table 5.

A potential re-entrant, stray-light path was identified: a fraction of the bright image of HI 121.6 nm on the detector will be reflected back toward the grating where it is diffracted again and imaged back onto the detector at a different apparent wavelength. The magnitude of this feature was estimated to be $\sim 15\%$ of the primary. It was found that a small tilt (4.2°) of the detector mount in the spectral dimension and toward the telescope (a right-hand turn about the EMUS -Y axis) would shift the re-entrant beam out of the active area with only a minor impact on imaging performance and all requirements still met. Another consequence is a slight increase in dispersion (lower RLD) to 2.66 nm mm^{-1} .

A light trap for the undispersed, zero-order light was precluded due to clearances required for the detector door and linkages (see Fig. 23). The zero-order beam is imaged outside the detector cavity, behind the aperture of the assembly in the open-door configuration, and onto the long arm linkage of its outboard side. Thus, the light is diffusely scattered by the conversion-coated aluminum throughout the spectrograph cavity. There was no obvious indication of detector backgrounds caused by this scatter in the ground calibration datasets.

5.3.3 Predicted Spectroscopic and Imaging Performance

Raytracing software was used to model the EMUS optical system and provide an estimate of imaging performance. Spectral resolution was determined by using an extended source

Fig. 10 The estimated spectral resolution for the HR slit meets the requirement of 1.5 nm at field angles across 140–170 nm. Simulations use an extended source that fills the aperture stop, slit width, and slit height

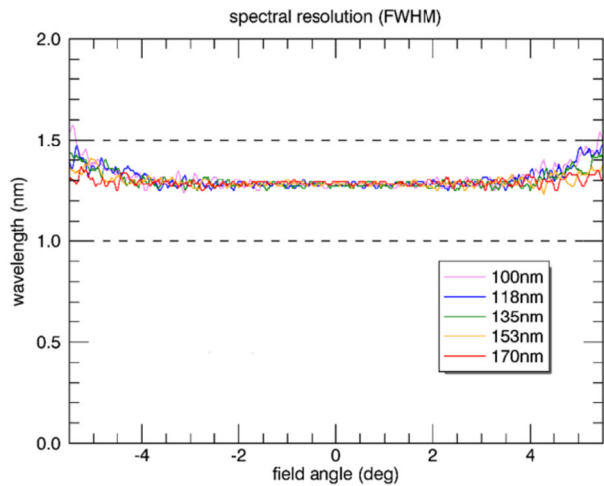
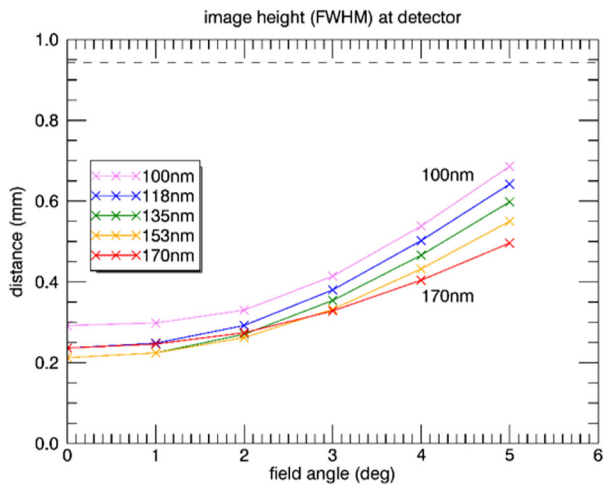


Fig. 11 The estimated image height is less than the required 0.36° (0.94 mm) at all wavelengths and field angles



that filled the aperture stop and HR entrance slit width and height. Five wavelengths were used across the required wavelength range. The simulated images were then convolved with an estimate of the detector point spread function, a two-dimensional Gaussian profile with conservative dimensions of 0.1×0.2 mm (spectral \times spatial) assumed early in development (actual dimensions turned out to be less and are given in §5.4.3). The FWHM of the simulated images at all field angles was calculated and a plot of the result is shown in Fig. 10. The spectral resolution is found to be less than the required 1.5 nm for all field angles across 140–170 nm.

Spatial resolution is determined by raytracing an extended object that fills the aperture stop and LR entrance slit width but only subtends 0.001° in the spatial dimension. Discrete images are produced at six field angles and five wavelengths; from these, the FWHM in the spatial dimension is calculated and shown in Fig. 11. The maximum image height ranges from 0.3 mm (0.11°) at 0° to 0.7 mm (0.27°) at 5° , thereby meeting the spatial resolution requirement of 0.36° .

5.3.4 Optical Substrates

The various challenges encountered in the procurement of low-roughness optical surfaces and the related difficulty in coating adhesion is out of scope for this paper; therefore, we will describe the components selected for flight here and the final coating application in the next section.

Cut, figured, and polished substrates for both the spherical telescope mirror and toroidal diffraction grating were procured from Precision Asphere (Fremont, CA). Precision surface metrology on the optical substrates was performed at Lawrence Livermore National Laboratory (LLNL) via Atomic Force Microscopy (AFM, using 10×10 , 5×5 , 2×2 , and $0.4\times 0.4\ \mu\text{m}^2$ frames) and optical profilometry ($2.5\times$ and $20\times$ magnifications, corresponding to $2.9\times 2.2\ \text{mm}^2$ and $0.37\times 0.28\ \text{mm}^2$ frames, respectively).

The substrate size of the telescope mirror is $42\times 68\ \text{mm}$ (spectral \times spatial), with a clear aperture of $35\times 61\ \text{mm}$. The optical figure is a sphere with a 300 mm radius of curvature and the substrate material is a low-thermal expansion glass-ceramic, O'Hara CLEARCERAM-Z HS, Class C3. The angle of incidence for an on-axis chief ray is 7° . The high-spatial frequency microroughness of the mirror substrates, defined here as the roughness corresponding to spatial lengths less than $2\ \mu\text{m}$, was determined by AFM to be at or below 0.2 nm rms. Late in the program it was discovered through optical profilometry measurements that the telescope mirror substrates exhibit sparsely distributed anomalous features characterized by shallow depressions ("pits") of average depth $\sim 10\text{--}20\ \text{nm}$ and width $\sim 100\text{--}200\ \text{nm}$. A comprehensive investigation into the distribution and frequency was not possible, but the limited spatial sampling seemed to indicate these features were widespread, randomly placed, and present on all telescope mirror substrates. No plausible mechanism of origin was identified. An analysis was conducted to determine the impact of these features on imaging performance; this consisted of modeling the pits as uniform circular depressions that redistribute light by its far-field Fourier transform, a Bessel function, weighted by their fractional area (~ 20 pits per $2.2 \times 3.0\ \text{mm}^2$ area or 2.38%) and convolved with the geometric image. The resulting scattered signal was found to be 10^{-4} (relative to the peak) and 10^{-5} at a distance of 0.5 mm and 1 mm, respectively. The measured near-field PSF of a smooth mirror (without pits) exhibited very similar performance as the simulation, demonstrating that the bidirectional reflectance distribution function (BRDF) from a polished optical surface contributes at least as much scatter as the anomalous pits. Negligible difference was found in the widths (FWHM) of simulated images with and without pits; therefore, the ability to meet the spatial resolution requirement is unchanged by the presence of these features.

The substrate size of the diffraction grating is $100\times 75\ \text{mm}$ (spectral \times spatial), and the clear aperture $87\times 59\ \text{mm}$. The optical figure is a toroid with radii of curvature 400.0 mm and 390.7 mm in the spectral and spatial dimensions, respectively. The grating substrate material is Corning 7980 Fused Silica, as requested by Horiba Jobin Yvon (France), the vendor providing the diffractive ruling.

The EMUS grating is of conventional type, with parallel grooves of constant spacing. The ruling density is $936\ \text{lines}\ \text{mm}^{-1}$ and the laminar groove profile (rectangular facets) is directly ion-etched into the glass substrate, parallel to its shorter side. This approach was selected because the traditional holographically-recorded sinusoidal profile uses a photoresist material that is incompatible with the cleaning process required in preparation of the substrate for SiC coating deposition. Inspection with the optical profilometer determined that the grating substrates were free of the "pit" features found on the mirror substrates. AFM metrology (2×2 and $0.4\times 0.4\ \mu\text{m}^2$ frames), obtained on top of the grating lines as well as the bottom of the grating grooves, determined that the microroughness was in the range

0.2–0.45 nm rms on the grating substrate ultimately selected for flight (see next subsection). The angle of incidence is 11° and the diffraction angle at 135 nm is 3.8° .

5.3.5 Optical Coatings

Most FUV instrumentation employ reflective optics coated with a layer of aluminum and a magnesium fluoride (MgF_2) protective overcoat; examples include the aforementioned instruments Cassini UVIS (FUV channel), MAVEN IUVS, and GOLD as well as the Lunar Reconnaissance Orbiter (LRO) Lyman-Alpha Mapping Project (LAMP) (Gladstone et al. 2010) and the Juno UltraViolet Spectrometer (UVS) (Gladstone et al. 2017). Bulk absorption by the MgF_2 layer, typically 25–40 nm thick, limits the useful wavelength range to $\gtrsim 115$ nm. The required spectral range for EMUS is 100–170 nm, and so we must consider alternative materials such as silicon carbide (SiC) or boron carbide (B4C), traditionally used in x-ray and EUV applications, that provide relatively high ($\sim 40\%$) reflectance at 100 nm. We selected SiC for its inherently lower compressive stress compared to B4C (Soufli et al. 2009) and optical properties similar to that of B4C at 100 nm. The gain in throughput at short wavelengths comes at the unacceptable cost of low throughput at longer wavelengths. In order to balance the competing needs in each wavelength range, the optical coatings on each element are divided into two equal areas of SiC and Al+ MgF_2 . A similar approach of “split” or “area-division” coatings was used by the Hinode (Solar-B) Extreme-Ultraviolet Imaging Spectrometer (EIS) (Korendyke et al. 2006), the Solar Dynamics Observatory (SDO) Atmospheric Imaging Array (AIA) (Lemen et al. 2012; Podgorski et al. 2009), and GOES space weather satellite Solar Ultraviolet Imager instruments (Martínez-Galarce et al. 2013).

The dividing line between the two coatings is parallel to the long axis of entrance slit, as can be seen in a picture of the flight-coated optics in Fig. 12. There is a narrow region (~ 2 mm) between the coatings that was not completely coated by either material and has indeterminate reflective properties. The coatings on the two optics are oriented such that light encountering one coating on the telescope mirror encounters the same on the grating. We chose the outboard side of the telescope mirror (EMUS frame -X) and the outboard side of the grating (EMUS frame +X) to be coated with Al+ MgF_2 ; this was motivated by the desire to reduce the magnitude of the re-entrant light path mentioned previously that primarily intersects the inboard side of the grating after reflection by the detector. For a point source located at infinity and oriented along the EMUS boresight, the projected beam of the aperture stop on the telescope mirror would illuminate equal areas of each coating; this is also true across the full range of field angles in the long-slit dimension (instrument Y-Z plane).

At angles in the cross-slit dimension (instrument X-Z plane) the projected beam does illuminate different fractional areas of the telescope mirror; however, because the angular width of the entrance slits is small, the change in throughput is minimal. For a point source oriented such that its image falls on one edge of the widest science slit width (0.67 mm or 0.26°), the projected beam from the aperture stop would be displaced from the center by 0.46 mm over the 206 mm distance. The fractional area of one coating over the other would differ by approximately 6% . This effect does not occur at the grating because it is coincident with the conjugate image of the aperture stop.

The optical coating group at Lawrence Livermore National Laboratory (LLNL), led by Regina Soufli, provided the SiC coatings as well as the precision surface metrology discussed in this and in the previous section, while Acton Optics provided the Al+ MgF_2 coating. A SiC coating thickness of 30–50 nm was specified.

A SiC coating with optimized roughness and stress properties developed by LLNL (Soufli et al. 2009) and deposited by DC magnetron sputtering was selected for the EMUS mirror

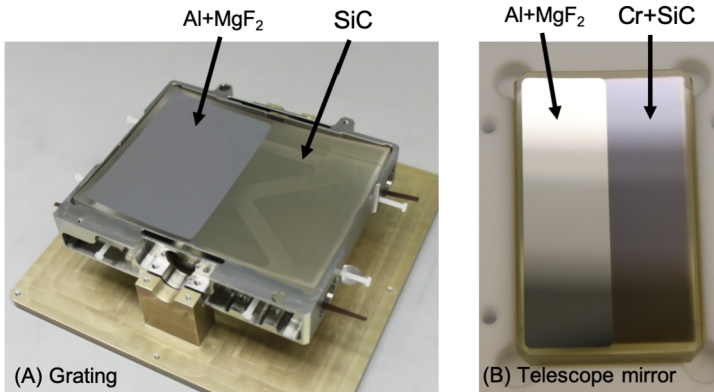


Fig. 12 Area division or “split” optical coatings are shown for the EMUS diffraction grating (A) and telescope mirror (B)

and grating. The stress of a 44.4 nm-thick SiC coating is -0.88 GPa (compressive) and the microroughness is 0.25 nm rms, when deposited on an “ideal” substrate (near-zero microroughness). To increase the probability of successful coating adhesion, an intermediate 6.6 nm-thick layer of chromium (Cr) was introduced between the reflective SiC coating and the substrate. The resulting stress of the [6.6+44.4] nm-thick Cr+SiC coating was -0.56 GPa and the microroughness 0.3 nm rms, with the reduction in compressive stress and slight increase in roughness attributed to the presence of Cr.

Coating of the telescope mirrors with Cr+SiC was conducted first. The SiC coating thickness on the flight mirror was measured on a test curved optic with identical geometry as the flight mirror, and was found to be 44.1 nm at the mirror center and 44.5 nm at a radius $r=30$ mm from the center. These thickness values were determined via reflectivity vs. angle measurements at a wavelength of 13.5 nm, performed at the Advanced Light Source beamline 6.3.2 located at Lawrence Berkeley National Laboratory (LBNL). As a validation of robustness, the coated optics were subjected to an environmental test consisting of ten thermal-vacuum cycles (TVAC) across a temperature range of -10°C to $+40^{\circ}\text{C}$. Visual inspection found that the coatings were unchanged.

One of the diffraction gratings was coated with a SiC-only coating while a second grating with a Cr+SiC coating. AFM metrology (5×5 and 2×2 μm^2 frames) showed that the rectangular facets of the SiC-only grating were only slightly modified by the coating, showing rounded corners, but the Cr+SiC-coated grating facets appeared trapezoidal. Due to the slightly higher efficiency of the un-coated grating substrate and the relatively unaltered facet profile of the SiC-only-coated grating, it was ultimately selected for installation in the flight instrument while the other grating was held in reserve as a backup spare. The flight grating was subjected to the TVAC cycling described above, though limited to three cycles due to schedule constraints, and subsequent inspection found that the coating was unchanged. The SiC coating thickness on the flight grating was measured via reflectivity vs. angle measurements on an un-ruled test curved optic with identical geometry as the flight grating, and was found to be 47 nm at the grating center and 47.7 nm at a radius $r=40$ mm from the center. AFM metrology (2×2 and 0.4×0.4 μm^2 frames) obtained at the top of the grating lines as well as at the bottom of the grating grooves after coating with SiC, determined that the microroughness was in the range 0.3–0.6 nm rms (it was 0.2–0.45 nm rms before coating). As

can be seen in Fig. 12, the coating of SiC on the grating is partially transparent to visible light; this does not alter in-band performance.

5.3.6 Predicted Radiometric Performance

The radiometric performance of the instrument is characterized by the measurement equation for the signal in counts at pixel (i,j):

$$C_{i,j} = L \cdot A_{AS} \cdot \frac{w_{slit} \cdot h_{pix}}{f^2} \cdot R_T \cdot R_G \cdot \eta \cdot QE_{det} \cdot \frac{d\lambda}{dx} \cdot w_{pix} \cdot dt \quad (8)$$

where:

- C: number of counts (detected photoevents)
- L: spectral radiance of the source
- A_{AS} : area of the aperture stop (30×20 mm)
- w_{slit} : slit width (0.48 mm HR slit, 0.67 mm LR slit)
- h_{pix} : detector pixel height (0.0264 mm average)
- f : focal length (150 mm)
- R_T : reflectance of the telescope mirror
- R_G : reflectance of the grating
- QE_{det} : detector quantum efficiency (counts per photoevent)
- η : grating diffraction efficiency, independent of coating reflectance
- $\frac{d\lambda}{dx}$: reciprocal linear dispersion
- w_{pix} : width of a pixel (0.0228 mm average)
- dt : integration period

A_{AS} , w_{slit} , h_{pix} , and f are geometric factors defined by the instrument design, and R_T , R_G , QE , η are wavelength-dependent parameters. As mentioned previously, the optics are oriented such that light encounters the same coating on each; therefore, the factor $R_T \cdot R_G$ is equal to half the sum of the squares of SiC and Al+MgF₂ reflectance. For the radiometric model we use the measured normal-incidence spectral reflectance of Al with a 25 nm thick protective layer of MgF₂ from Bradford et al. (1969) (longer wavelengths) and Hunter et al. (1971) (shorter wavelengths). QE is a measured response of the cesium iodide (CsI) photocathode provided by the UC Berkeley Space Sciences Laboratory (UCB-SSL), η is calculated based on the grating design parameters and provided by Horiba Jobin Yvon (JY). Each estimated component efficiency is shown in Fig. 13 and the filled-slit sensitivity for the HR slit and a 0.36° spatial element is shown in Fig. 14.

5.4 Detector Description

The EMUS detector is a photon-counting, open-face microchannel plate (MCP) imaging device with a cross-delay line (XDL) anode readout provided by UCB-SSL. The detector electronics is a hybrid of SSL implementations used in the GOLD instrument (McClintock et al. 2020; Siegmund et al. 2016) and the Ionospheric Connection Explorer Extreme Ultraviolet spectrometer (ICON-EUV) (Sirk et al. 2017). The MCP stack, detector body, and enclosure are identical to that used by GOLD, except: the MCP rectangular active area mask was replaced by a larger circular mask, the circular UV transmissive window in the reclosable door was replaced by a larger rectangular one to accommodate the oblique illumination from the internal lamp, and the pump port aperture was enlarged to increase conductance.

Fig. 13 Fractional, spectral efficiencies of each component used in the EMUS radiometric model

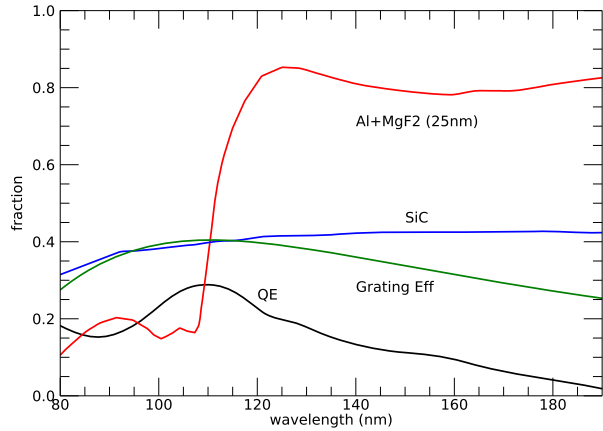
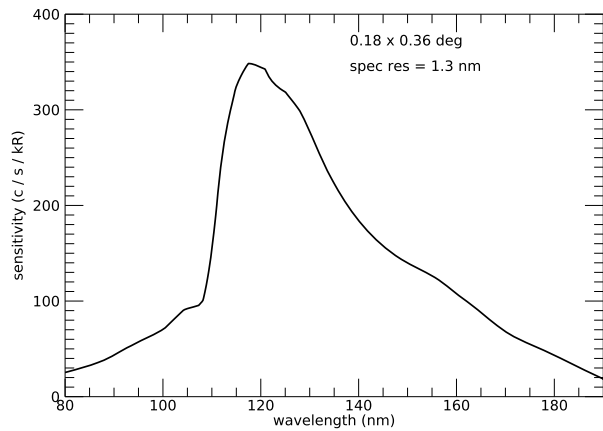


Fig. 14 EMUS spectral sensitivity estimate from the radiometric model for a 0.36° spatial resolution element and a filled HR slit



5.4.1 Operation

Photons entering the detector will first pass through a QE enhancement grid with 95% open area, located ~ 6 mm above the front surface of the MCP that is coated with $\sim 1 \mu\text{m}$ of cesium iodide (CsI). In-band photons will interact with the CsI producing a photoelectron that is subsequently amplified by the MCP stack (a triplet set of 46 mm diameter, 19° bias angle MCPs with $12 \mu\text{m}$ pores on $15 \mu\text{m}$ centers and 60:1 length to diameter ratio, arranged in a Z-stack configuration). The circular 38 mm diameter active area of the detector is defined by a thin metal aperture placed between the bottom two MCPs in the stack. The pore bias angle and clocking orientation in the instrument were selected to optimize the detector QE across the EMUS bandpass. The QE enhancement grid is maintained at a voltage more negative than the top of the MCPs, thus providing for collection of any photoelectrons emitted from the inter-pore region of the MCP surface. Electrons are accelerated down the MCP pores by a high voltage potential maintained across the MCPs. Interaction of these electrons with the walls of the MCP pores results in a stochastic amplification process, with an ultimate gain determined by the voltage applied across the MCPs. The positional information of the incident photon is maintained through the amplification process.

A bias of 400 V across the 6 mm gap between the MCP output surface and the XDL anode provides an accelerating field for the output cloud of electrons onto the anode. The charge cloud is collected by two sets of cross patterned, serpentine delay lines. The signal produced on a single line propagates in opposite directions, and the difference in arrival time at each end determines the position. But first, the four signals (two for each axis) exit the detector body to be processed by the detector electronics, located – by necessity of close proximity – directly behind the detector and inside the spectrograph cavity (see Fig. 5). The signals are amplified, and for each axis, an analog voltage is produced by a time-to-amplitude converter (TAC) circuit, which is then digitized along with the charge pulse amplitude. The X and Y position of each photoevent is encoded to 12 bits, resulting in a 4096×4096 data space, while the pulse amplitude, P, is encoded to 8 bits. An FPGA controls the processing and transmits the 32-bit value (X, Y, P) to the EMUS EBox.

The relationship between encoded pixel position and real space varies with temperature, resulting in both a shift and stretch. To assist in developing a correction to the data, two external electronic stimulus sources or “stims” are injected into the anode to produce point sources outside of the MCP active area at diagonal corners. The rate at which the stims are active is commandable, with a typical value during science observations of 20 Hz (10 Hz each); thus, an integration of one second would result in 10 counts at each stim location. Stim positions are provided with every detector image read out.

A fundamental characteristic of the detector is the QE dependency on gain (“QE-gain curve”). Above a certain gain value, the QE has only a slight positive dependence with gain; below, some photoevents in the charge distribution fall below the detection threshold of the XDL electronics and are lost from the image, an effective decrease in QE. We optimized the electronics performance about a modal gain value of ~ 1 pC (6.2×10^6 e-) to balance detector lifetime and resolution capabilities.

5.4.2 Nonlinearity Correction

Photoevents are processed one at a time, and during this finite period, known as the “dead time”, the detector is unable to respond to subsequent events. The probability of this occurring increases with the total count rate across the entire detector. This effect was measured by Berkeley SSL up to a count rate of ~ 300 kHz, and the dead time found to be 750 ns. The relationship between the observed count rate, CR_o , the dead time τ , and the true count rate CR_t is given by:

$$CR_t = \frac{CR_o}{1 - CR_o \tau} \quad (9)$$

Although photoevents occurring within the dead time cannot be located, they are counted by the Fast Event Counter (FEC) circuit characterized by a much shorter dead time (125 ns). This FEC value is reported in the telemetry for every science image. Therefore, there are two independent methods for correcting the nonlinear behavior of detector response at high count rates. We estimate the maximum possible count rate to be 236 kHz based on a uniformly-filled low-resolution slit with a 15 kilorayleigh (kR) H I 121.6 nm radiance, and a 1 kR radiance at O I 130.4 nm. (The rayleigh unit is used to specify both a column emission rate and an apparent radiance such that 1 rayleigh is equivalent to $10^6/(4\pi)$ photons $\text{sec}^{-1} \text{cm}^{-2} \text{ster}^{-1}$, Baker and Romick 1976) This would result in an observed count rate of 200 kHz, necessitating a correction of 1.17. The uncertainty in this correction is estimated to be $< 1\%$.

A second source of potential nonlinearity is local in nature. If the irradiance (count rate per unit area) of a source is too high, the resupply current in the MCP cannot be provided quickly enough. The effect is a depression of the gain in that region, and thus is known as “gain sag”. If the local modal gain is depressed far enough (below ~ 0.4 pC) a fraction of pulses from the anode will fall below the detection threshold of the electronics and result in loss of counts. This effect is expected to become detectable at a signal of 3 counts s^{-1} micropore $^{-1}$. At 15 kR, the maximum predicted brightness of H I 121.6 nm, the estimated signal is 2.2 counts s^{-1} micropore $^{-1}$. Calibration stars are chosen to avoid gain sag.

5.4.3 Spatial Imaging

Discretized photoevent positions in two dimensional space can be conceptualized as “pixels”. Photoevent positions are encoded with 12 bits in each axis, therefore the detector provides an array of 4096×4096 pixels. The corresponding physical location of these pixels, and the size of the pixels themselves, is characterized during detector development by placing a mechanical mask with an array of $10 \mu\text{m}$ holes on 1 mm centers onto the bare MCP and illuminated by a lamp. The average pixel size was found to be $22.94 \times 26.34 \mu\text{m}$ (spectral \times spatial). A number of effects in the detector electronics introduce non-linearities in the mapping of the image plane to the reported position of the charge clouds by the electronics; the distortions are stable and the residual deviation from a fitted low-order polynomial was found to be a maximum of $\pm 50 \mu\text{m}$ in the X axis and $\pm 25 \mu\text{m}$ in the Y axis.

The detector PSF was also found using the pinhole mask data. At each location, a one-dimensional Gaussian distribution was fit to the summed profile in each direction at an average gain of ~ 1 pC. The average dimensions were found to be $0.08 \times 0.08 \text{ mm}$ (spectral \times spatial) FWHM.

Within the 38 mm diameter active area of the detector, the required wavelength range of 100–170 nm spans a 26.3 mm detector width, and the 10.75° field a height of 28.9 mm. Because of the circular boundary, the minimum and maximum possible wavelengths are a function of field angle; at the center horizontal chord of the detector subtends ~ 83 –180 nm. The bounding wavelength range with field angle is also a function of the grating-yaw mechanism (GYM), a mechanism that rotates the grating about an axis normal to the dispersion plane and described later in more detail.

5.4.4 Gain Stabilization

Except during operation in vacuum with the detector door open, the detector cavity was filled with dry nitrogen throughout all ground activities to protect against exposure to water vapor (see §5.6.10). Over time, the interior surfaces of MCP micropores adsorb N_2 gas molecules that alter their gain properties. As the detector is illuminated, the cascading electrons impacting the walls of the micropores will desorb these molecules. This results in a decline of gain within the detector’s illuminated region, with a rate proportional to the cumulative extracted charge, measured in units of coulomb cm^{-2} . Eventually, the gain falls below the electronics detection threshold and counts are lost. Unmitigated, this effect would create a problem for the highly-structured spectral/spatial images to be acquired by EMUS: the bright H I 121.6 nm emission line could “burn” itself into the detector to the point where that region becomes unresponsive, while the weaker lines decline at a slower rate.

A process known as “scrubbing” is used to stabilize the gain across the active area of the detector, preventing the differential burn-in effect described above. Because the detector cavity is filled with dry N_2 at the time of launch, this operation must occur in flight. The

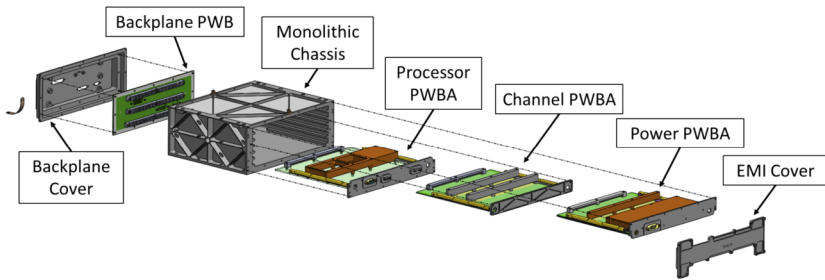


Fig. 15 Exploded view of EMUS EBox

internal lamp (§5.6.9) provides the stimulus required for this activity. The relevant emission wavelength from the lamp is at 184.9 nm, where the detector QE is a few percent (bright emissions exist at longer wavelengths, particularly at 253.7 nm, but the detector QE is many orders of magnitude lower). A scrub procedure was conducted according to that described by Darling et al. (2017) and references therein, early in the cruise phase of the mission. (A detailed description of this activity and subsequent results is beyond the scope of this paper.) Afterward, the operational voltage is adjusted to maintain an average gain of ~ 1 pC per photoevent across the required region of the detector; by maintaining a consistent position on the QE-gain curve (§5.4.1), the measured, pre-launch radiometric sensitivity is still applicable. Flight calibrations using well-characterized stars will be used to validate the sensitivity.

5.5 Electronics Box (EBox) Design

5.5.1 Overview

The EMUS Electronics Box (EBox) is the electrical interface between the EMUS spectrograph and the EMM spacecraft, providing the power, control, and processing required to operate the detector electronics, high voltage power supply, flat-field lamp, mechanisms, operational heater, and solar safety sensor. The EBox is mounted on the +Y main instrument panel of the EMM spacecraft and consists of a processor printed wire board assembly (PWBA), power PWBA, channel control PWBA, and backplane enclosed in a light-weighted 23.6×24.9×9.7 cm monolithic aluminum chassis with EMI and backplane close-outs. The EBox mass is 3.2 kg. See Fig. 15 for an exploded view of the EMUS EBox.

The processor PWBA is built around an RTAX2000 FPGA that contains an embedded 8051 microcontroller core (Core8051) supplied by Microsemi Corporation. In addition to providing the command and data interface to the spacecraft, the processor board controls all of the subsystems within the spectrograph. These interfaces include:

- Detector electronics: power on/off, reset on/off, stim pulse on/off, fauxton generator on/off, photon (X, Y, pulse height) processing and storage, fast event counter (FEC) accumulation
- High voltage power supply (HVPS): power on/off, output enable/disable, adjustable output
- Flat-field lamp: power on/off
- For all mechanisms (RAD, slit, GYM, detector door): power on/off, direction clockwise/counter-clockwise, adjustable number of steps, adjustable step rate, adjustable phase

- Operational heater: power on/off, adjustable temperature setpoint
- Solar safety sensor (SSS): adjustable trigger threshold
- Science telemetry to spacecraft: 5 MHz LVDS
- Commanding from spacecraft: 115.2 kbps RS-422
- Housekeeping telemetry to spacecraft: 115.2 kbps RS-422

The processor PWBA hosts two 512K×16 SRAM integrated circuits (ICs) for storage and execution of system code and for microprocessor data memory; two 4M×16 NOR Flash ICs for non-volatile storage of boot code, operational code, and parameter tables; and two 64M×32 SDRAM ICs for storage of uncompressed science data resulting from photoevent processing.

The channel control PWBA hosts the power switches for the detector electronics and mechanism Hall effect sensors; opto-isolated solid state relays for the mechanism stepper motors; and analog control circuitry for the operational heater. The power PWBA contains a low voltage power supply that converts regulated spacecraft power to the various voltages required for all of the subassemblies; power switches for HVPS, mechanism control circuitry, the flat-field lamp, and the operational heater; and ADCs and a MUX for sampling the various analog telemetry items throughout the instrument. Analog telemetry items include voltages, currents, and temperatures.

5.5.2 Photon and Image Processing

An EMUS “observation” consists of a sequence of images obtained with a fixed instrument configuration, defined by the following parameters: image window, binning, stim windows, pulse height window, integration time, compression block size, number of images, mechanism position (RAD, detector door, GYM, slit), flat field lamp state, and detector voltage. Only events within the image window are stored in science memory. Binning is specified in each direction independently, and must be a power of two. The two stim windows, of dimension up to 32×32 detector pixels, are notionally centered on the detector stims. A pulse height histogram is produced for all events that occur within the pulse height window for every detector readout.

For each photoevent registered by the detector electronics, the event location (X, Y) and pulse height (PH) information is transmitted to the processor PWBA for further processing. The FPGA has three data storage modes that process and store photoevents in the following ways:

1. Binned-Deep (Counts Only): The science data memory is organized such that each memory address corresponds to an accumulator for each science bin defined by the photon processing parameters above. The size of each accumulator is 26 bits and represents the number of photon detections (counts) in a particular science bin. No photon PHs are stored in this mode. Each accumulator is protected by 6 bits of error detector and correction (EDAC). The maximum number of accumulators in this mode is 128M.
2. Binned Wide (Counts + Pulse Heights): The science data memory is organized such that each memory address corresponds to two accumulators for each science bin defined by the photon processing parameters above. Each accumulator size is 26 bits and one represents the number of photon detections (counts) in a particular science bin, while the other represents the cumulative PH of each photoevent in that science bin. Each accumulator is protected by 6 bits of error detector and correction (EDAC). The maximum number of accumulators in this mode is 64M.

3. List Mode: The science data memory is a list of the X location (12 bits), Y location (12 bits), and pulse height (8 bits) of each photoevent that has been received from the detector electronics. The details of each received photon is protected by 7 bits of EDAC. At the end of each integration period an incrementing marker, corresponding to a region outside the active area, is inserted into the list. The maximum number of addresses in this mode is 64M.

All science observations will use the Binned-deep acquisition mode, while all calibration observations will use Binned-wide. List mode results in a large volume of data, but provides maximum insight into detector behavior. For the calibration observation that involves observing the internal lamp to characterize variations in spatial or temporal sensitivity, a short (1 sec) period of list mode data is acquired after a set of observations in Binned-wide.

5.5.3 Compression

Once the integration time associated with the first image in memory has elapsed, flight software (FSW) reads and compresses the windowed/binning images, one at a time. The FAST algorithm (Rice 1983) works by reducing the bit depth of the data to only what is required within the compression block size, N , a configurable parameter for each observation that can take a value of 8, 16, or 32. The processing steps are:

1. Select block of N science bins within a spatial column.
2. Determine the number of bits, B , required to represent the maximum value in the block and truncate each 26 bit accumulator to B bits.
3. Write the 8-bit value of B followed by the N truncated, B -bit accumulators into the science data packet.
4. Continue with the next block of N science bins in the image.

To prevent the block from containing data in multiple columns, the number of bins in the spatial dimension must be a multiple of N . For blocks that contain only zeros, only the value $B=0$ is written into the packet.

This compression technique excels when the block of data contains similar values and where bright features are largely confined to a small number of columns; EMUS data generally satisfies both of these conditions. Compression is applied to counts images and PH images, but not list mode data.

5.6 Spectrograph Components and Subsystems

5.6.1 Overview

The EMUS Spectrograph is a single-piece, machined aluminum optical bench, plus cover, mounted to the spacecraft deck using 6 titanium struts arranged in 3 bipods. The stiffness of each strut is tuned with helical cuts to provide vibration isolation for sensitive optical components and mechanisms. The following is a description of the major components and subsystems within the spectrograph, and identified in Fig. 5.

5.6.2 Solar Safety Sensor

The Solar Safety Sensor (SSS) consists of a photodiode behind a circular aperture, mounted to the front of the instrument (Fig. 5) and aligned with the telescope boresight. If the Sun

Fig. 16 The EMUS RAD subassembly protects the optics against exposure to the Sun between observations

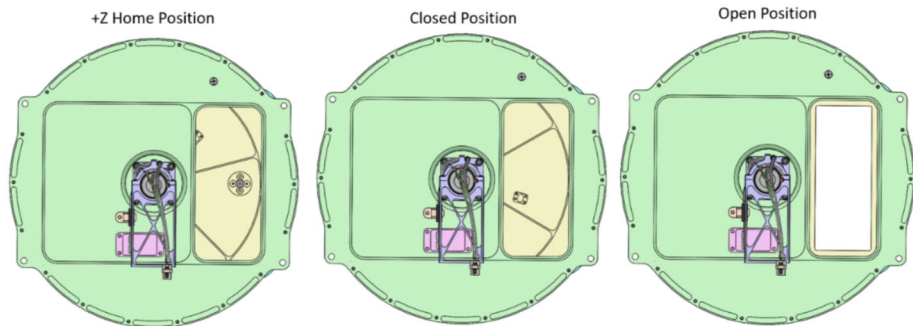
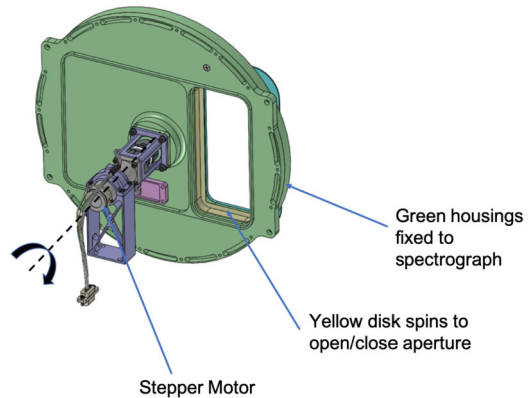


Fig. 17 The EMUS RAD is used in three discrete states: a closed home position, a second closed position used during operations, and the open position used for observations

enters the 31.8° (full cone angle, FWHM) FOV, a signal threshold circuit will trigger the instrument to enter safe mode, closing the reclosable aperture door (RAD) and turning off the detector high voltage. This trigger is disabled when the RAD is closed, allowing the Sun to pass through the SSS FOV without incident. Nominal operations planning prevents the EMUS boresight from being pointed within 19° from the Sun during active observations; therefore, the SSS would only be triggered due to an anomalous condition.

5.6.3 Reclosable Aperture Door

The reclosable aperture door (RAD) serves as a contamination control door during instrument and spacecraft integration and test and as way to only expose the EMUS optics to space during planned observations. In addition, it has the functionality of quickly closing to protect the optics if the Sun approaches the field-of-view during an EMUS observation. The RAD consists of a rotating disk with a cutout that aligns with a housing, with a corresponding cutout that is attached to the spectrograph. The mechanism is driven by a stepper motor controlled by the EBox. The RAD subassembly can be seen Fig. 16, while the various RAD positions can be see in Fig. 17.

Fig. 18 Light enters the EMUS telescope assembly through the aperture stop, reflecting from the split-coated mirror, and forms an image onto one of the slit apertures actuated into position by a rotational mechanism

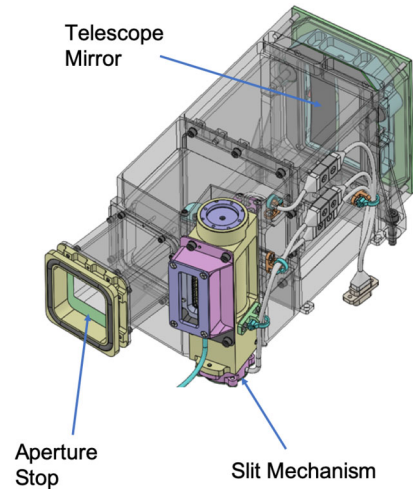


Table 6 EMUS slit widths with measurement uncertainties

Slit name	Uncertainty (+/-%)	Physical width (mm)	Spectral width (nm)	Spatial width (degrees)
Very-high resolution (VHR)	10.5%	0.1209	0.325	0.046
High resolution (HR)	2.6%	0.4822	1.297	0.184
Low resolution (LR)	3.8%	0.6729	1.810	0.257
Very-low resolution (VLR)	1.4%	1.8491	4.974	0.706

5.6.4 Telescope Assembly

The telescope assembly consists of an aperture stop, a telescope mirror (see Fig. 12), and a slit mechanism. Light enters through the aperture stop and is focused by the telescope mirror on the slit. The telescope assembly can be seen in Fig. 18.

5.6.5 Slit Mechanism

The heritage slit mechanism uses a frameless, 15° stepper motor to actuate a carousel that positions one of four slit apertures, listed in Table 6, into the telescope focal plane. The slit mechanism can be seen in Fig. 19.

5.6.6 Ion Repeller Grids

Ion repeller grids (IRG) are used at both entrances to the optical cavity: after the slit mechanism and before the ascent vent. Each IRG is held at a voltage that is 1/27th of the detector QEG voltage; for example, with QEG at 4000 V the IRG potential would be 148 V. The purpose of the IRGs is to limit the influx of low-energy positive ions into the spectrograph cavity where they can induce a detector background signal. While we do not anticipate this

Fig. 19 The EMUS slit mechanism positions one of four slit apertures into the telescope focal plane

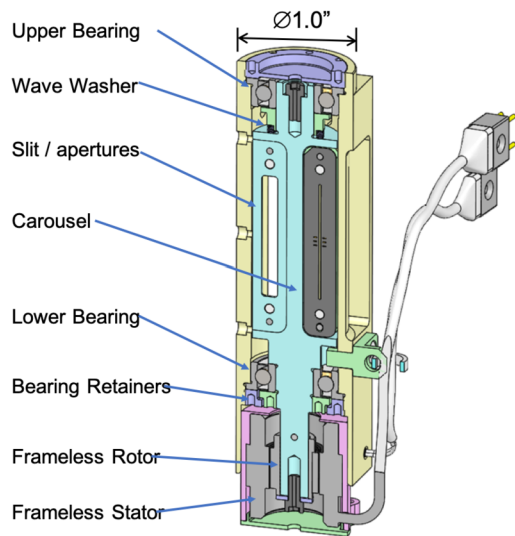
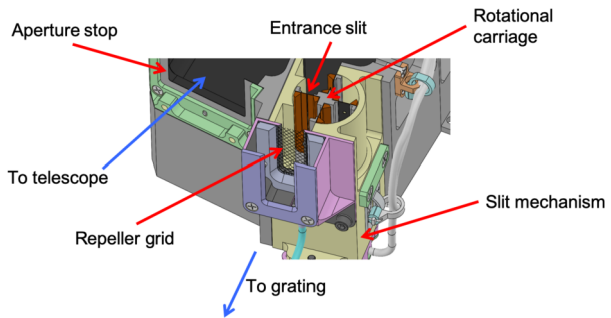


Fig. 20 The EMUS slit Ion Repeller Grid (IRG) follows the slit mechanism in the light path, and exhibits 95% transmissivity



to be a significant effect at the high-altitude orbit of the Hope probe, the IRGs were implemented for simplicity from the heritage assembly design. The IRGs consist of 0.00127 inch diameter wires in a mesh arrangement with a spacing of 20 per inch. At 95% transmissivity, the slit IRG has minimal impact on throughput. The slit IRG can be seen in Fig. 20 and the ascent vent and associated IRG can be seen in Fig. 21.

5.6.7 Ascent Vent

The ascent vent provides a path for the filtered air, used to purge the rocket fairing, within the spectrograph cavity to exit during launch. A labyrinthian path frustrates external light from entering the spectrograph, with a minimum of 14 scattering events. A cross section of the ascent vent is shown in Fig. 21.

5.6.8 Grating Yaw Mechanism (GYM)

The grating-yaw mechanism (GYM) is a heritage subsystem and uses a stepper-based cam actuator to shift the image on the detector in the spectral dimension. This will be used for a routine calibration activity where the image at H I 121.6 nm is displaced and measured

Fig. 21 Cross section of the EMUS ascent vent. The Ion Repeller Grid (IRG) at the top faces the spectrograph interior while the perforated surface at the bottom has an unobstructed view away from the spacecraft

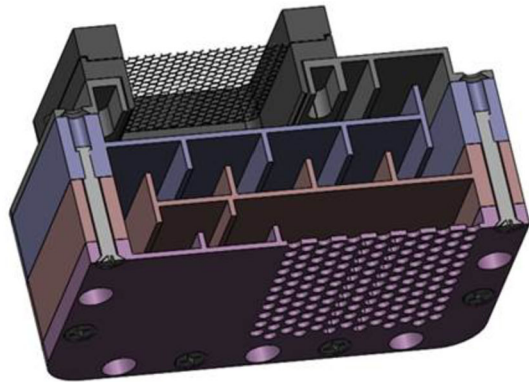
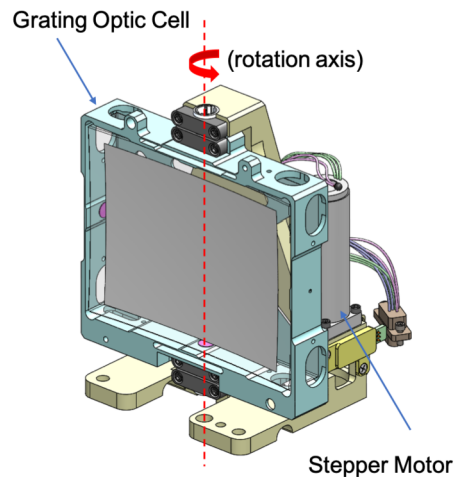


Fig. 22 The EMUS Grating-Yaw Mechanism (GYM) rotates the diffraction grating about its central axis (parallel to its grooves), displacing the image at the focal plane in the spectral dimension



on either side of its nominal position to look for any changes in detector response from this persistent, high flux source. The GYM can be seen in Fig. 22.

5.6.9 Internal Lamp

A low-pressure mercury lamp is included within the EMUS spectrograph cavity and located on the outboard side of the diffraction grating, allowing an unobstructed, if somewhat oblique, view of the detector. The primary purpose of the lamp is to provide the stimulus required for the gain-stabilization or “scrub” procedure described in §5.4.4. The secondary purpose is to provide global illumination of the entire detector active area in order to characterize temporal changes in sensitivity. The lamp can be seen in Fig. 5.

5.6.10 Detector Enclosure

The CsI photocathode is subject to degradation when exposed to water vapor (Xie et al. 2012). Because of this, special care has been taken to avoid contact with ambient air of any relative humidity level. As seen in Fig. 23, the detector body mates to a vacuum housing with an o-ring seal. A reclosable door mechanism attaches to the vacuum housing such that

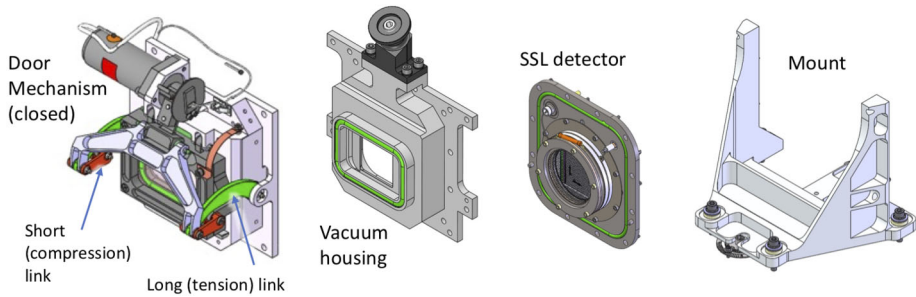


Fig. 23 EMUS detector subassembly components

the door engages an o-ring on the housing. Strict controls during instrument assembly, integration, and test (AI&T), developed during the GOLD mission, protect any inadvertent exposure of the detector to ambient air. Because of the high voltage exposed in the open-face detector, it can only be operated in a vacuum environment. At the conclusion of any measurements, the vacuum chamber containing the detector subassembly or instrument is backfilled with dry nitrogen, also filling the detector cavity, and the detector door closed. Upon completion of final ground testing and calibration in Nov. 2019, the detector cavity was pumped out through a port at the top of the vacuum housing (see Fig. 23), and dry N_2 gas re-introduced at 5 psi above ambient pressure to prevent air ingress. Testing of an engineering model (EM) detector assembly in this configuration showed no detectable reduction in pressure over a time period of a week, while another test showed no pressure decrease throughout a vibration test.

As the lamp is far too bright to be observed at operational (photon-locating) gain, a neutral density (ND) filter with optical density value of 4.9 (transmittance of 1.3×10^{-5}) is included in the detector door to limit the count rate to ~ 200 kHz for this characterization. To prevent the build-up of desorbed gas within the detector cavity, these measurements are conducted with the door at a position 5° from closed, called the “flat-field” position.

5.7 Thermal Subsystem

Both the spectrograph and EBox are almost completely covered with multi-layer insulation (MLI) and will maintain fairly stable temperatures throughout the early operations, during detector scrub, and the science phase of the mission. Using the operational heater mounted beneath the optical bench, during early operation we anticipate holding the detector temperature at $+28^\circ\text{C}$ with less than 0.5 W of operational heater power. During science phase, we anticipate holding the detector at $+26 \pm 1^\circ\text{C}$ with less than 7 W of operational heater power.

6 Measurement Performance

The Multiple Optical Beam Instrumentation (MOBI) facility at LASP was used to determine the fundamental performance characteristics of the completed EMUS instrument. MOBI consists of a large vacuum chamber (~ 50 inch diameter) into which is installed the instrument mounted to a four-axis (pitch, yaw, vertical, horizontal) pointing platform. The telescope is directed toward an off-axis parabola (OAP) with a focal length of 2.286 meters. At the focus of the OAP a variety of optical sources can be mounted, and the system provides a collimated beam that overfills the EMUS 30×20 mm entrance aperture.

6.1 Absolute Radiometric Sensitivity

The EMUS absolute calibration was determined by measuring the instrument response to a collimated light source of known brightness at three monochromatic wavelengths and five field angles. The light source consists of a McPherson 629 windowless hollow-cathode lamp (HCL), fed by one of several available gases (O_2 , N_2 , H_2), the output of which is coupled to a McPherson 234/302 scanning-grating monochromator and its exit slit placed at the focus of the MOBI OAP.

A photomultiplier tube (PMT) with CsI photocathode and MgF_2 window was used as a secondary transfer detector, whose QE response was measured against a photodiode calibrated at the National Institute of Standards and Technology (NIST). The PMT transfer detector was placed in the same plane as the EMUS entrance aperture. For any measurement at a given wavelength, the quasi-monochromatic beam was spatially scanned by the PMT using the MOBI pointing platform to characterize its uniformity and measure the flux. The EMUS entrance pupil was then centered in the beam and a measurement obtained at field angles of -5.0 , -2.5 , 0 , 2.5 , and 5.0° .

The signal count rate from the reference detector is proportional to the incident irradiance (photon rate per unit area) multiplied by the limiting aperture area (0.95 cm diameter) and its QE. Because the EMUS telescope image underfills the VLR entrance slit used in this activity, the same relationship applies and the absolute instrumental quantum throughput (counts per photon entering the FOV) can be derived from the ratio of responses of the two detector systems:

$$QE_{EMUS} = \frac{CR_{EMUS}/A_{EMUS}}{CR_{ref}/A_{ref}} QE_{ref} \quad (10)$$

where CR_{EMUS} is the count rate from EMUS, A_{EMUS} is the area of the EMUS entrance pupil, CR_{ref} is the count rate from the reference PMT detector, A_{ref} is the area of the reference detector aperture, and QE_{ref} is the QE of the reference detector. Referring to Eq. 8, QE_{EMUS} is equivalent to a combination of parameters: $R_T \cdot R_G \cdot \eta \cdot QE_{det}$. The product of A_{EMUS} and QE_{EMUS} is known as the “effective area”, another common radiometric performance quantity.

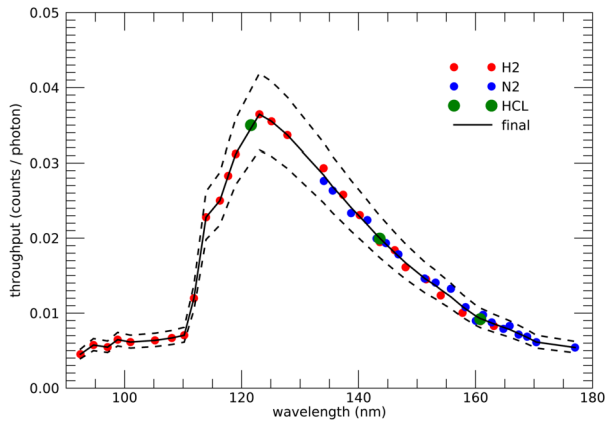
H_2 gas was used to feed the HCL, and the monochromator used to select prominent emission lines at 121.6, 143.6, 160.8 nm for calibration. A measurement was also conducted at 102.6 nm using a bare (no photocathode), open-face MCP as the calibrated reference detector; however, ions present in the vacuum chamber, presumably originating from the HCL, produced a large detector background that precluded a reliable measurement. Observations were conducted in photon-list mode. The pointing platform was used to articulate EMUS about its entrance pupil, drifting a monochromatic image across the VLR slit at a rate of $\sim 0.001^\circ \text{ sec}^{-1}$ and images acquired every 1 sec (defined by time markers in the photon list data stream). All data points acquired while the image was contained within the slit (chosen for repeatability and convenience to be where the image was located within 80% of the angular FWHM) were averaged together for a single measurement at a particular wavelength and field position. The final absolute sensitivity values, averaged across all field angles and obtained after instrument environmental testing, are given in Table 7. The variation across field angle is less than 3% for all wavelengths.

6.2 Relative Radiometric Sensitivity

Complementing the discrete absolute data points, we make use of the relative calibration technique described by Ajello et al. (1988). An electron gun was installed inside the MOBI

Table 7 Post-environmental absolute sensitivity measurements

Wavelength (nm)	Counts per photon	Random uncertainty
121.60	0.035	2.1%
143.60	0.020	1.3%
160.80	0.0092	1.7%

Fig. 24 The final, composite radiometric throughput is indicated by the solid black curve, while the dashed curves indicate an estimated systematic uncertainty of $\pm 15\%$. The relative response components from the e-gun lamp using N_2 and H_2 gases, and the absolute values measured with the HCL are indicated

vacuum chamber and located ~ 4 meters in front of the instrument; at this finite distance, the emitting region of the lamp forms an out of focus image at the EMUS telescope focal plane. In the wavelength range 92–163 nm we make use of H_2 source gas with a beam energy of 100 eV. Using the emission spectral model from Liu et al. (2000), Jonin et al. (2000) and provided by Ajello (2017), we calculate the ratio of integrated signal within each of 27 resolved features to those of the model, convolved to match the EMUS spectral resolution. A similar process is used with a source gas of N_2 at a beam energy of 30 eV, stimulating emission from the Lyman-Birge-Hopfield (LBH) band system, and providing 20 features in the wavelength range 134–177 nm.

The two independently-derived relative sensitivity curves were normalized to each other in the overlapping wavelength range of 133–164 nm. Data points were sorted by wavelength to create an aggregate spectral response curve. The LOWESS (LOcally WEighted Scatterplot Smoother) function was applied to the values above 125 nm and joined with the lower wavelength data.

6.3 Final Radiometric Sensitivity

The ratio of the three absolute sensitivity values from Table 7 to those interpolated from the processed, relative response curve was calculated. The average of these ratios was used to scale the relative curve, creating the continuous, absolute spectral radiometric sensitivity of the EMUS instrument. This curve, along with the scaled values from the H_2 and N_2 measurements, and the three absolute values obtained with the HCL are shown in Fig. 24. An estimated systematic uncertainty of $\pm 15\%$ is indicated as dashed lines.

6.4 System Point Spread Function

The dataset described in § 6.1 was used to determine the PSF of the system at four wavelengths and five field angles. As a monochromatic image in the telescope focal plane is

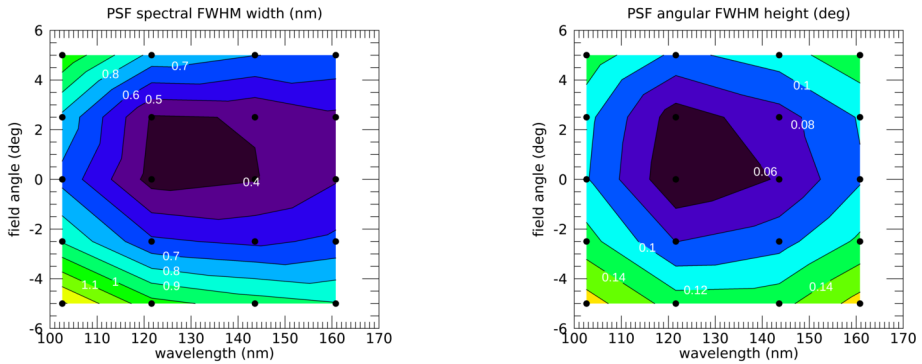


Fig. 25 The left plot shows the spectral width of the system PSF across most of the required spectral and spatial ranges. The right plot shows the PSF spatial height in degrees across the same range

drifted across the slit, detector images are created from the photon stream in time ranges of 4 seconds. A Gaussian function is then fit to the spectral and spatial profile of each detector image, and the parameters averaged for the period where the telescope image is fully contained within the entrance slit. We derive the FWHM from these fit parameters in the spectral and spatial dimensions, and contour plots of each are shown in Fig. 25.

The spectral width ranges from ~ 0.4 nm at the center to ~ 1.2 nm in the bottom left corner (low wavelength, negative field angles). These values correspond to unresolved point sources such as stars, while the spectral resolution of extended sources (i.e. the Mars atmosphere) is defined by the convolution of this system spectral width with that of the entrance slit image.

The spatial height ranges from 0.06° at the center to 0.16° in the bottom left and right corners.

6.5 Line Spread Function, Spectroscopic Resolution, and Spatial Imaging

The dataset described in §6.1 was used to determine the Line Spread Function (LSF) of the system at four wavelengths and five field angles. Instead of the data reduction method described in §6.4, a single, summed image was derived from each of the swaths of the monochromatic image across each slit, thereby synthesizing a source that fills the angular subtense. For each of the resulting images, the FWHM is calculated in the spectral and spatial dimensions. The former characterizes the LSF and thus the effective spectral resolution of the instrument. The results are shown as annotated contour plots in Fig. 26. The spectral width is less than the requirement of 1.5 nm for all field angles across 140–170 nm, while the spatial image height meets the 0.36° requirement, ranging from 0.04° to 0.16° , nearly identical (as expected) to the values found from the PSF.

6.6 Wavelength Range

The wavelength scale, the association of wavelength with detector location, was characterized by measuring the centroid pixel location of features from the relative calibration dataset and comparing them to the wavelength location of the same features in the model. The average RLD was found to be 2.65 nm mm^{-1} , slightly lower (higher dispersion) than the expected value of 2.66 nm mm^{-1} derived in 5.3.2.

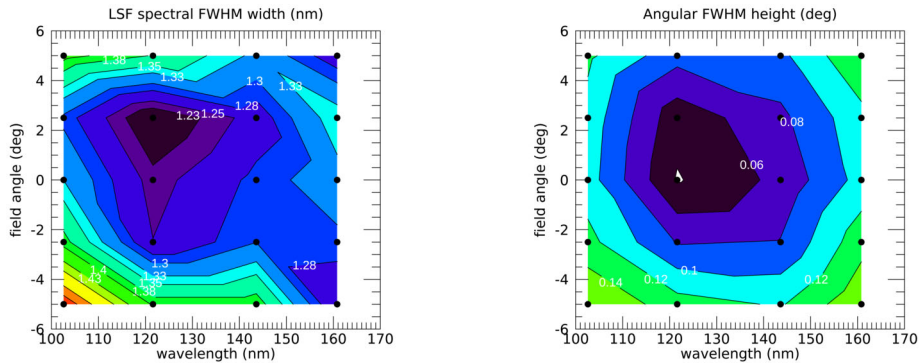


Fig. 26 EMUS line spread function (LSF) width (spectral resolution) for the HR slit (left) and spatial image size (right)

It was found that high distortion and buildup of charge at edge of the MCP mask complicated both the wavelength scale and radiometric characterization in this region, the exclusion of which decreases the useful detector area to a circle of diameter ~ 36 mm. At a GYM position of 152, a wavelength range of 100–163 nm is achieved across the full 10.75° spatial range. Away from the ends of slit, toward smaller field angles, the wavelength range increases to a maximum of 83–180 nm at the 0° center chord.

The longest-wavelength feature of the CO 4PG system identified for measurement occurs at 163 nm, but a maximum wavelength of 170 nm is specified so that a local minimum in emission can be observed to characterize scattering and detector backgrounds. This objective will be accomplished across most of the spatial range, and so is not strictly required at the extreme ends of the FOV.

7 Conclusion

EMUS is an ultraviolet imaging spectrograph onboard the EMM Hope probe, which entered orbit around Mars in Feb 2021. The instrument will obtain routine observations of key atomic and molecular emissions from the Mars thermosphere and exosphere with comprehensive spatial coverage at sub-seasonal timescales. Using these measurements, EMUS will investigate how conditions throughout the Mars atmosphere affect rates of atmospheric escape, and how key constituents in the exosphere behave temporally and spatially. The EMUS hardware implementation makes use of several heritage subsystems. A set of measurement requirements that enable the science investigations have been shown to be met through a comprehensive calibration program.

Acknowledgements The EMUS instrument was made possible by the many committed engineers, technicians, managers, and support staff at CU-LASP and MBRSC. Two anonymous reviewers provided comments and suggestions that substantially improved this manuscript. We are grateful to Tom Pardini (LLNL) for the precision surface metrology measurements, Jeff Robinson (LLNL) for thin film depositions, Jay Ayers (LLNL) for coating fixture design and Eric Gullikson (LBNL) for the reflectance measurements at 13.5 nm. The SiC optical coating work was performed under the auspices of the U.S. Department of Energy by Lawrence Livermore National Laboratory under Contract No. DE-AC52-07NA27344. Funding for LLNL was provided by LASP/University of Colorado via a Work-for-Others agreement.

Funding Funding for development of the EMM mission was provided by the UAE government, and to co-authors outside of the UAE by MBRSC.

Declarations

Compliance with Ethical Standards The authors have complied with the ethical standards of Space Science Reviews in preparing this manuscript and conducting any analysis described therein.

Conflict of Interest The authors declare that they have no conflict of interest.

Ethical approval The authors approve the ethical standards declaration above.

Informed consent All authors have been informed of and agreed to the submission of this manuscript.

Open Access This article is licensed under a Creative Commons Attribution 4.0 International License, which permits use, sharing, adaptation, distribution and reproduction in any medium or format, as long as you give appropriate credit to the original author(s) and the source, provide a link to the Creative Commons licence, and indicate if changes were made. The images or other third party material in this article are included in the article's Creative Commons licence, unless indicated otherwise in a credit line to the material. If material is not included in the article's Creative Commons licence and your intended use is not permitted by statutory regulation or exceeds the permitted use, you will need to obtain permission directly from the copyright holder. To view a copy of this licence, visit <http://creativecommons.org/licenses/by/4.0/>.

References

- J. Ajello, Private communication (2017)
- J.M. Ajello, D.E. Shemansky, B. Franklin, J. Watkins, S. Srivastava, G.K. James, W.T. Simms, C.W. Hord, W. Pryor, W. McClintock, V. Argabright, D. Hall, Simple ultraviolet calibration source with reference spectra and its use with the Galileo orbiter ultraviolet spectrometer. *Appl. Opt.* **27**, 890–914 (1988). <https://doi.org/10.1364/AO.27.000890>. <http://www.osapublishing.org/ao/abstract.cfm?uri=ao-27-5-890>
- H. AlMatroushi, H. AlMazmi, N. AlMheiri, M. AlShamsi, E. AlTunaiji, K. Badri, R. Lillis, F. Lootah, M. Yousuf, H.E.S. Amiri, D.A. Brain, M. Chaffin, J. Deighan, C.S. Edwards, F. Forget, M.D. Smith, M.J. Wolff, P. Christensen, S. England, M. Fillingim, G.M. Holsclaw, S.K. Jain, A. Jones, M. Osterloo, B.M. Jakosky, J.G. Luhmann, R.M.B. Young, Emirates Mars mission characterization of Mars atmosphere dynamics and processes. *Space Sci. Rev.* (2021). <https://doi.org/10.1007/s11214-021-00851-6>
- H.E.S. Amiri, D. Brain, O. Sharaf, P. Withnell, M. McGrath, M. AlAwadhi, H. AlMatroushi, Z. AlShamsi, O. AlShehhi, M. Chaffin, J. Deighan, C. Edwards, N. Ferrington, B. Harter, G. Holsclaw, M. Kelley, D. Kubitschek, H. Landin, R. Lillis, M. Packard, J. Parker, E. Pilinski, B. Pramman, H. Reed, S. Ryan, C. Sanders, M. Smith, R. Wrigley, H. AlMazmi, N. AlMheiri, M. AlShamsi, E. AlTunaiji, K. Badri, P. Christensen, S. England, M. Fillingim, F. Forget, S.K. Jain, B.M. Jakosky, A. Jones, F. Lootah, J.G. Luhmann, M. Osterloo, M. Wolff, M. Yousuf, The emirates Mars mission. *Space Sci. Rev.* (2021), this journal. SPAC-D-20-00145
- D.E. Anderson Jr., C.W. Hord, Mariner 6 and 7 ultraviolet spectrometer experiment: analysis of hydrogen Lyman-alpha data. *J. Geophys. Res.* **76**, 6666 (1971). <https://doi.org/10.1029/JA076i028p06666>
- D.J. Baker, G.J. Romick, The Rayleigh: interpretation of the unit in terms of column emission rate or apparent radiance expressed in SI units. *Appl. Opt.* **15**(8), 1966–1968 (1976). <https://doi.org/10.1364/AO.15.001966>. <http://www.osapublishing.org/ao/abstract.cfm?uri=ao-15-8-1966>
- C.A. Barth, J.B. Pearce, K.K. Kelly, L. Wallace, W.G. Fastie, Ultraviolet emissions observed near Venus from Mariner V. *Science* **158**, 1675–1678 (1967). <https://doi.org/10.1126/science.158.3809.1675>
- C.A. Barth, W.G. Fastie, C.W. Hord, J.B. Pearce, K.K. Kelly, A.I. Stewart, G.E. Thomas, G.P. Anderson, O.F. Raper, Mariner 6 and 7: ultraviolet spectrum of Mars upper atmosphere. *Science* **165**, 1004–1005 (1969)
- C.A. Barth, C.W. Hord, J.B. Pearce, K.K. Kelly, G.P. Anderson, A.I. Stewart, Mariner 6 and 7 ultraviolet spectrometer experiment: upper atmosphere data. *J. Geophys. Res.* **76**, 2213–2227 (1971). <https://doi.org/10.1029/JA076i010p02213>
- C.A. Barth, A.I. Stewart, C.W. Hord, A.L. Lane, Mariner 9 ultraviolet spectrometer experiment: Mars airglow spectroscopy and variations in Lyman alpha. *Icarus* **17**, 457–462 (1972). [https://doi.org/10.1016/0019-1035\(72\)90011-5](https://doi.org/10.1016/0019-1035(72)90011-5)

- A. BenMoussa, S. Gissot, U. Schühle, G. Del Zanna, F. Auchère, S. Mekaoui, A.R. Jones, D. Walton, C.J. Eyles, G. Thuillier, D. Seaton, I.E. Dammasch, G. Cessateur, M. Meftah, V. Andretta, D. Berghmans, D. Bewsher, D. Bolsée, L. Bradley, D.S. Brown, P.C. Chamberlin, S. Dewitte, L.V. Didkovsky, M. Dominique, F.G. Eparvier, T. Foujols, D. Gillotay, B. Giordanengo, J.P. Halain, R.A. Hock, A. Irbah, C. Jeppesen, D.L. Judge, M. Kretzschmar, D.R. McMullin, B. Nicula, W. Schmutz, G. Ucker, S. Wieman, D. Woodraska, T.N. Woods, On-orbit degradation of solar instruments. *Sol. Phys.* **288**(1), 389–434 (2013). <https://doi.org/10.1007/s11207-013-0290-z>
- J.L. Bertaux, O. Korabiev, S. Perrier, E.Q. merais, F. Montmessin, F. Leblanc, S. Lebonnois, P. Rannou, F. Lefère, F. Forget, A. Fedorova, E. Dimarellis, A. Reberac, D. Fonteyn, J.Y. Chaufray, S. Guibert, SPICAM on Mars Express: observing modes and overview of UV spectrometer data and scientific results. *J. Geophys. Res.* **111**(E10), 10 (2006). <https://doi.org/10.1029/2006JE002690>
- D. Bhattacharyya, J.T. Clarke, J.Y. Chaufray, M. Mayyasi, J.L. Bertaux, M.S. Chaffin, N.M. Schneider, G.L. Villanueva, Seasonal changes in hydrogen escape from Mars through analysis of HST observations of the Martian exosphere near perihelion. *J. Geophys. Res. Space Phys.* **122**(11), 11,756–11,764 (2017). <https://doi.org/10.1002/2017JA024572>
- S.W. Bougher, T.E. Cravens, J. Grebowsky, J. Luhmann, The aeronomy of Mars: characterization by MAVEN of the upper atmosphere reservoir that regulates volatile escape. *Space Sci. Rev.* **195**, 423–456 (2015a). <https://doi.org/10.1007/s11214-014-0053-7>
- S.W. Bougher, D. Pawlowski, J.M. Bell, S. Nelli, T. McDunn, J.R. Murphy, M. Chizek, A. Ridley, Mars global ionosphere-thermosphere model: solar cycle, seasonal, and diurnal variations of the Mars upper atmosphere. *J. Geophys. Res.* **120**(2), 311–342 (2015b). <https://doi.org/10.1002/2014JE004715>
- A.P. Bradford, G. Hass, J.F. Osantowski, A.R. Toft, Preparation of mirror coatings for the vacuum ultraviolet in a 2-m evaporator. *Appl. Opt.* **8**(6), 1183 (1969). <https://doi.org/10.1364/AO.8.001183>. <https://www.osapublishing.org/abstract.cfm?URI=ao-8-6-1183>
- M.S. Chaffin, J. Chaufray, I. Stewart, F. Montmessin, N.M. Schneider, J. Bertaux, Unexpected variability of martian hydrogen escape. *Geophys. Res. Lett.* **41**(2), 314–320 (2014). <https://doi.org/10.1002/2013GL058578>
- M.S. Chaffin, J.Y. Chaufray, J. Deighan, N.M. Schneider, W.E. McClintock, A.I.F. Stewart, E. Thiemann, J.T. Clarke, G.M. Holsclaw, S.K. Jain, M.M.J. Crismani, A. Stiepen, F. Montmessin, F.G. Eparvier, P.C. Chamberlain, B.M. Jakosky, Three-dimensional structure in the Mars H corona revealed by IUVS on MAVEN. *Geophys. Res. Lett.* **42**, 9001–9008 (2015). <https://doi.org/10.1002/2015GL065287>
- M.S. Chaffin, J.Y. Chaufray, J. Deighan, N.M. Schneider, M. Mayyasi, J.T. Clarke, E. Thiemann, S.K. Jain, M.M.J. Crismani, A. Stiepen, F.G. Eparvier, W.E. McClintock, A.I.F. Stewart, G.M. Holsclaw, F. Montmessin, B.M. Jakosky, Mars H escape rates derived from MAVEN/IUVS Lyman alpha brightness measurements and their dependence on model assumptions. *J. Geophys. Res. Space Phys.* **123**, 2192–2210 (2018). <https://doi.org/10.1029/2018JE005574>
- M.S. Chaffin, D.M. Kass, S. Aoki, A.A. Fedorova, J. Dieghan, K. Connour, N.G. Heavens, A. Kleinbohl, S.K. Jain, J.Y. Chaufray, M. Mayyasi, J.T. Clarke, A.I.W. Stewart, J.S. Evans, M.H. Stevens, M. McClintock, M. Crismani, G.M. Holsclaw, F. Lefevre, D.Y. Lo, F. Montmessin, N.M. Schneider, B. Jakosky, G. Villanueva, G. Liuzzi, F. Daerden, I.R. Thomas, J.J. Lopez-Moreno, M.R. Patel, G. Bellucci, B. Ristic, J.T. Erwin, A.C. Vandaele, A. Trokhmovskiy, O.I. Korabiev, Martian water loss to space enhanced by regional dust storms. *Nat. Astron.* **5**, 1036–1042 (2021). <https://doi.org/10.1038/s41550-021-01425-w>
- J.W. Chamberlain, Planetary coronae and atmospheric evaporation. *Planet. Space Sci.* **11**(8), 901–960 (1963). [https://doi.org/10.1016/0032-0633\(63\)90122-3](https://doi.org/10.1016/0032-0633(63)90122-3)
- J.Y. Chaufray, J.L. Bertaux, F. Leblanc, E. Quémerais, Observation of the hydrogen corona with SPICAM on Mars Express. *Icarus* **195**(2), 598–613 (2008). <https://doi.org/10.1016/j.icarus.2008.01.009>
- J.T. Clarke, J.L. Bertaux, J.Y. Chaufray, G.R. Gladstone, E. Quémérais, J.K. Wilson, D. Bhattacharyya, A rapid decrease of the hydrogen corona of Mars. *Geophys. Res. Lett.* **41**(22), 8013–8020 (2014). <https://doi.org/10.1002/2014GL061803>
- C. Cox, J.C. Gérard, B. Hubert, J.L. Bertaux, S.W. Bougher, Mars ultraviolet dayglow variability: SPICAM observations and comparison with airglow model. *J. Geophys. Res.* **115**, E04010 (2010). <https://doi.org/10.1029/2009JE003504>
- N.T. Darling, O.H.W. Siegmund, T. Curtis, J. McPhate, J. Tedesco, S. Courtade, G. Holsclaw, A. Hoskins, S.A. Dhafri, Microchannel plate life testing for UV spectroscopy instruments, in *UV, X-Ray, and Gamma-Ray Space Instrumentation for Astronomy XX*, vol. 10397 (SPIE, Bellingham, 2017), p. 1039712. <https://doi.org/10.1117/12.2277343>. <http://www.spiedigitallibrary.org/conference-proceedings-of-spie/10397/1039712/Microchannel-plate-life-testing-for-UV-spectroscopy-instruments/10.1117/12.2277343.short>
- J. Deighan, M.S. Chaffin, J.Y. Chaufray, A.I.F. Stewart, N.M. Schneider, S.K. Jain, A. Stiepen, M. Crismani, W.E. McClintock, J.T. Clarke, G.M. Holsclaw, F. Montmessin, F.G. Eparvier, E.M.B. Thiemann, P.C. Chamberlain, B.M. Jakosky, MAVEN IUVS observation of the hot oxygen corona at Mars. *Geophys. Res. Lett.* **42**, 9009–9014 (2015). <https://doi.org/10.1002/2015GL065487>

- N.N. Dementyeva, V.G. Kurt, A.S. Smirnov, L.G. Titarchuk, S.D. Chuvahin, Preliminary results of measurements of UV emissions scattered in the Martian upper atmosphere. *Icarus* **17**, 475 (1972)
- L.W. Esposito, C.A. Barth, J.E. Colwell, G.M. Lawrence, W.E. McClintock, A.I.F. Stewart, H.U. Keller, A. Korth, H. Lauche, M.C. Festou, A.L. Lane, C.J. Hansen, J.N. Maki, R.A. West, H. Jahn, R. Reulke, K. Warlich, D.E. Shemansky, Y.L. Yung, The Cassini Ultraviolet Imaging Spectrograph investigation. *Space Sci. Rev.* **115**(1), 299–361 (2004). <https://doi.org/10.1007/s11214-004-1455-8>
- J.S. Evans, D.J. Strickland, R.E. Huffman, Satellite remote sensing of thermospheric O/N₂ and solar EUV. 2: data analysis. *J. Geophys. Res.* **100**, 12227 (1995). <https://doi.org/10.1029/95JA00573>
- J.S. Evans, M.H. Stevens, J.D. Lumpe, N.M. Schneider, A.I.F. Stewart, J. Deighan, S.K. Jain, M.S. Chaffin, M. Crismani, A. Stiepen, W.E. McClintock, G.M. Holsclaw, F. Lefèvre, D.Y. Lo, J.T. Clarke, F. Eparvier, E.M.B. Thiemann, F. Montmessin, B.M. Jakosky, Retrieval of CO₂ and N₂ in the Martian thermosphere using dayglow observations by IUVS on MAVEN. *Geophys. Res. Lett.* **42**, 9040–9049 (2015). <https://doi.org/10.1002/2015GL065489>
- P.D. Feldman, E.B. Burgh, S.T. Durrance, A.F. Davidsen, Far-ultraviolet spectroscopy of Venus and Mars at 4 Å resolution with the Hopkins Ultraviolet Telescope on Astro-2. *Astrophys. J.* **538**, 395–400 (2000). <https://doi.org/10.1086/309125>
- P.D. Feldman, H.A. Weaver, E.B. Burgh, Far ultraviolet spectroscopic explorer observations of CO and H₂ emissions in comet C/2001 A2(Linear). *Astrophys. J. Lett.* **576**, L91–L94 (2002)
- P.D. Feldman, A.J. Steffl, J.W. Parker, M.F. A'Hearn, J.L. Bertaux, S. Alan Stern, H.A. Weaver, D.C. Slater, M. Versteeg, H.B. Throop, N.J. Cunningham, L.M. Feaga, Rosetta-Alice observations of exospheric hydrogen and oxygen on Mars. *Icarus* **214**(2), 394–399 (2011). <https://doi.org/10.1016/j.icarus.2011.06.013>
- G.R. Gladstone, S.A. Stern, K.D. Retherford, R.K. Black, D.C. Slater, M.W. Davis, M.H. Versteeg, K.B. Persson, J.W. Parker, D.E. Kaufmann, A.F. Egan, T.K. Greathouse, P.D. Feldman, D. Hurley, W.R. Pryor, A.R. Hendrix, LAMP: the Lyman alpha mapping project on NASA's lunar reconnaissance orbiter mission. *Space Sci. Rev.* **150**(1), 161–181 (2010). <https://doi.org/10.1007/s11214-009-9578-6>
- G.R. Gladstone, S.C. Persyn, J.S. Eterno, B.C. Walther, D.C. Slater, M.W. Davis, M.H. Versteeg, K.B. Persson, M.K. Young, G.J. Dirks, A.O. Sawka, J. Tumlinson, H. Sykes, J. Beshears, C.L. Rhoad, J.P. Cravens, G.S. Winters, R.A. Klar, W. Lockhart, B.M. Pieggrass, T.K. Greathouse, B.J. Trantham, P.M. Wilcox, M.W. Jackson, O.H.W. Siegmund, J.V. Vallergera, R. Raffanti, A. Martin, J.C. Gérard, D.C. Grodent, B. Bonfond, B. Marquet, F. Denis, The ultraviolet spectrograph on NASA's Juno mission. *Space Sci. Rev.* **213**(1), 447–473 (2017). <https://doi.org/10.1007/s11214-014-0040-z>
- F. González-Galindo, M.A. López-Valverde, F. Forget, M. García-Comas, E. Millour, L. Montabone, Variability of the Martian thermosphere during eight Martian years as simulated by a ground-to-exosphere global circulation model. *J. Geophys. Res.* **120**(11), 2020–2035 (2015). <https://doi.org/10.1002/2015JE004925>
- G. Gronoff, C.S. Wedlund, C.J. Mertens, M. Barthélemy, R.J. Lillis, O. Witasse, Computing uncertainties in ionosphere-airglow models. II — the Martian airglow. *J. Geophys. Res.* **117**, A05309 (2012). <https://doi.org/10.1029/2011JA017308>
- H. Haber, The torus grating. *J. Opt. Soc. Am.* **40**(3), 153 (1950). <https://doi.org/10.1364/JOSA.40.000153>. <https://www.osapublishing.org/abstract.cfm?URI=josa-40-3-153>
- R.R. Hodges, F.S. Johnson, Lateral transport in planetary exospheres. *J. Geophys. Res. Space Phys.* **73**(23), 7307 (1968). <https://doi.org/10.1029/JA073i023p07307>
- M.C.E. Huber, G. Tondello, Stigmatic performance of an EUV spectrograph with a single toroidal grating. *Appl. Opt.* **18**(23), 3948 (1979). <https://doi.org/10.1364/AO.18.003948>. <https://www.osapublishing.org/abstract.cfm?URI=ao-18-23-3948>
- W.R. Hunter, J.F. Osantowski, G. Hass, Reflectance of aluminum overcoated with MgF₂ and LiF in the wavelength region from 1600 Å to 300 Å at various angles of incidence. *Appl. Opt.* **10**(3), 540 (1971). <https://doi.org/10.1364/AO.10.000540>. <https://www.osapublishing.org/abstract.cfm?URI=ao-10-3-540>
- S.K. Jain, Dayglow Emissions on Mars and Venus. Ph.D. thesis, Cochin University of Science and Technology, India (2013). <https://dyuthi.cusat.ac.in/jspui/bitstream/purl/3688/1/Dyuthi-T1654.pdf>
- S.K. Jain, A.I.F. Stewart, N.M. Schneider, J. Deighan, J.S. Evans, M.H. Stevens, M.S. Chaffin, M. Crismani, W.E. McClintock, J.T. Clarke, G.M. Holsclaw, D.Y. Lo, F. Lefèvre, F. Montmessin, E.M.B. Thiemann, F. Eparvier, B.M. Jakosky, The structure and variability of Mars upper atmosphere as seen in MAVEN/IUVS dayglow observations. *Geophys. Res. Lett.* **42**, 9023–9030 (2015). <https://doi.org/10.1002/2015GL065419>
- S.K. Jain, S.W. Bougher, J. Deighan, N.M. Schneider, F. González Galindo, A.I.F. Stewart, R. Sharrar, D. Kass, J. Murphy, D. Pawlowski, Martian thermospheric warming associated with the planet encircling dust event of 2018. *Geophys. Res. Lett.* **47**(3), e2019GL085302 (2020). <https://doi.org/10.1029/2019GL085302>
- B.M. Jakosky, R.P. Lin, J.M. Grebowsky, J.G. Luhmann, D.F. Mitchell, G. Beutelschies, T. Priser, M. Acuna, L. Andersson, D. Baird, D. Baker, R. Bartlett, M. Benna, S. Bougher, D. Brain, D. Carson, S. Cauffman,

- P. Chamberlin, J.Y. Chaufray, O. Cheatom, J. Clarke, J. Connerney, T. Cravens, D. Curtis, G. Delory, S. Demcak, A. DeWolfe, F. Eparvier, R. Ergun, A. Eriksson, J. Easley, X. Fang, D. Folta, J. Fox, C. Gomez-Rosa, S. Habenicht, J. Halekas, G. Holsclaw, M. Houghton, R. Howard, M. Jarosz, N. Jedrich, M. Johnson, W. Kasprzak, M. Kelley, T. King, M. Lankton, D. Larson, F. Leblanc, F. Lefevre, R. Lillis, P. Mahaffy, C. Mazelle, W. McClintock, J. McFadden, D.L. Mitchell, F. Montmessin, J. Morrissey, W. Peterson, W. Pospel, J.A. Sauvaud, N. Schneider, W. Sidney, S. Sparacino, A.I.F. Stewart, R. Tolson, D. Toubanc, C. Waters, T. Woods, R. Yelle, R. Zurek, The Mars Atmosphere and Volatile Evolution (MAVEN) mission. *Space Sci. Rev.* **195**, 3–48 (2015). <https://doi.org/10.1007/s11214-015-0139-x>
- R.E. Johnson, M.R. Combi, J.L. Fox, W.H. Ip, F. Leblanc, M.A. McGrath, V.I. Shematovich, D.F. Strobel, J.H. Waite, Exospheres and atmospheric escape. *Space Sci. Rev.* **139**(1–4), 355–397 (2008). <https://doi.org/10.1007/s11214-008-9415-3>
- C. Jonin, X. Liu, J.M. Ajello, G.K. James, H. Abgrall, High-resolution electron-impact emission spectrum of H₂. I. cross sections and emission yields 900–1200 Å. *Astrophys. J. Suppl. Ser.* **129**(1), 247 (2000). <https://doi.org/10.1086/313414>. <http://iopscience.iop.org/article/10.1086/313414/meta>
- C.M. Korendyke, C.M. Brown, R.J. Thomas, C. Keyser, J. Davila, R. Hagood, H. Hara, K. Heidemann, A.M. James, J. Lang, J.T. Mariska, J. Moser, R. Moye, S. Myers, B.J. Probyn, J.F. Seely, J. Shea, E. Shepler, J. Tandy, Optics and mechanisms for the Extreme-Ultraviolet Imaging Spectrometer on the Solar-B satellite. *Appl. Opt.* **45**(34), 8674 (2006). <https://doi.org/10.1364/AO.45.008674>. <https://www.osapublishing.org/abstract.cfm?URI=ao-45-34-8674>
- V.A. Krasnopolsky, Mars' upper atmosphere and ionosphere at low, medium, and high solar activities: implications for evolution of water. *J. Geophys. Res.* **107**(E12), 5128 (2002). <https://doi.org/10.1029/2001JE001809>
- F. Leblanc, J.Y. Chaufray, J. Lilensten, O. Witasse, J.L. Bertaux, Martian dayglow as seen by the SPICAM UV spectrograph on Mars Express. *J. Geophys. Res.* **111**, E09S11 (2006). <https://doi.org/10.1029/2005JE002664>
- J.R. Lemen, A.M. Title, D.J. Akin, P.F. Boerner, C. Chou, J.F. Drake, D.W. Duncan, C.G. Edwards, F.M. Friedlaender, G.F. Heyman, N.E. Hurlburt, N.L. Katz, G.D. Kushner, M. Levay, R.W. Lindgren, D.P. Mathur, E.L. McFeaters, S. Mitchell, R.A. Rehse, C.J. Schrijver, L.A. Springer, R.A. Stern, T.D. Tarbell, J.P. Wuelser, C.J. Wolfson, C. Yanari, J.A. Bookbinder, P.N. Cheimets, D. Caldwell, E.E. Deluca, R. Gates, L. Golub, S. Park, W.A. Podgorski, R.I. Bush, P.H. Scherrer, M.A. Gummin, P. Smith, G. Auker, P. Jerram, P. Pool, R. Soufli, D.L. Windt, S. Beardsley, M. Clapp, J. Lang, N. Waltham, The Atmospheric Imaging Assembly (AIA) on the Solar Dynamics Observatory (SDO), in *The Solar Dynamics Observatory*, ed. by P. Chamberlin, W.D. Pesnell, B. Thompson (Springer, New York, 2012), pp. 17–40. https://doi.org/10.1007/978-1-4614-3673-7_3
- R.J. Lillis, D.A. Brain, S.W. Bougher, F. Leblanc, J.G. Luhmann, B.M. Jakosky, R. Modolo, J. Fox, J. Deighan, X. Fang, Y.C. Wang, Y. Lee, C. Dong, Y. Ma, T. Cravens, L. Andersson, S.M. Curry, N. Schneider, M. Combi, I. Stewart, J. Clarke, J. Grebowsky, D.L. Mitchell, R. Yelle, A.F. Nagy, D. Baker, R.P. Lin, Characterizing atmospheric escape from Mars today and through time, with MAVEN. *Space Sci. Rev.* **195**(1–4), 357–422 (2015). <https://doi.org/10.1007/s11214-015-0165-8>
- X. Liu, D.E. Shemansky, J.M. Ajello, D.L. Hansen, C. Jonin, G.K. James, High-resolution electron-impact emission spectrum of H₂. II. 760–900 Å. *Astrophys. J. Suppl. Ser.* **129**, 267–280 (2000). <https://doi.org/10.1086/313413>. <http://adsabs.harvard.edu/abs/2000ApJS..129..267L>
- M.A. López-Valverde, J.C. Gerard, F. González-Galindo, A.C. Vandaele, I. Thomas, O. Korablev, N. Ignatiev, A. Fedorova, F. Montmessin, A. Määttänen, S. Guilbon, F. Lefevre, M.R. Patel, S. Jiménez-Monferrer, M. García-Comas, A. Cardesin, C.F. Wilson, R.T. Clancy, A. Kleinböhl, D.J. McCleese, D.M. Kass, N.M. Schneider, M.S. Chaffin, J.J. López-Moreno, J. Rodríguez, Investigations of the Mars upper atmosphere with ExoMars trace gas orbiter. *Space Sci. Rev.* **214**(1), 29 (2018). <https://doi.org/10.1007/s11214-017-0463-4>
- P.R. Mahaffy, M. Benna, T. King, D.N. Harpold, R. Arvey, M. Barciniak, M. Bendt, D. Carrigan, T. Errigo, V. Holmes, C.S. Johnson, J. Kellogg, P. Kimvilakani, M. Lefavor, J. Hengemihle, F. Jaeger, E. Lyness, J. Maurer, A. Melak, F. Noreiga, M. Noriega, K. Patel, B. Prats, E. Raaen, F. Tan, E. Weidner, C. Gundersen, S. Battel, B.P. Block, K. Arnett, R. Miller, C. Cooper, C. Edmonson, J.T. Nolan, The neutral gas and ion mass spectrometer on the Mars atmosphere and volatile evolution mission. *Space Sci. Rev.* **195**(1–4), 49–73 (2015). <https://doi.org/10.1007/s11214-014-0091-1>
- D.S. Martínez-Galarce, R. Soufli, D.L. Windt, M.E. Bruner, E.M. Gullikson, S. Khatri, E.A. Spiller, J.C. Robinson, S.L. Baker, E. Prast, Multisegmented, multilayer-coated mirrors for the Solar Ultraviolet Imager. *Opt. Eng.* **52**(9), 095102 (2013). <https://doi.org/10.1117/1.OE.52.9.095102> <http://www.spiedigitallibrary.org/journals/optical-engineering/volume-52/issue-9/095102/Multisegmented-multilayer-coated-mirrors-for-the-Solar-Ultraviolet-Imager/10.1117/1.OE.52.9.095102.short>
- W.E. McClintock, N.M. Schneider, G.M. Holsclaw, J.T. Clarke, A.C. Hoskins, I. Stewart, F. Montmessin, R.V. Yelle, J. Deighan, The Imaging Ultraviolet Spectrograph (IUVS) for the MAVEN mission. *Space Sci. Rev.* **195**, 75–124 (2015). <https://doi.org/10.1007/s11214-014-0098-7>

- W.E. McClintock, R.W. Eastes, A.C. Hoskins, O.H.W. Siegmund, J.B. McPhate, A. Krywonos, S.C. Solomon, A.G. Burns, Global-scale observations of the limb and disk mission implementation: 1. Instrument design and early flight performance. *J. Geophys. Res. Space Phys.* **125**(5), e2020JA027797 (2020). <https://doi.org/10.1029/2020JA027797>. <https://onlinelibrary.wiley.com/doi/pdf/10.1029/2020JA027797>
- M.B. McElroy, J.C. McConnell, Atomic carbon in the atmospheres of Mars and Venus. *J. Geophys. Res.* **76**(28), 6674–6690 (1971). <https://doi.org/10.1029/JA076i028p06674>
- A.F. Nagy, J. Kim, T.E. Cravens, Hot hydrogen and oxygen atoms in the upper atmospheres of Venus and Mars. *Ann. Geophys.* **8**, 251–256 (1990)
- M.R. Patel, P. Antoine, J. Mason, M. Leese, B. Hathi, A.H. Stevens, D. Dawson, J. Gow, T. Ringrose, J. Holmes, S.R. Lewis, D. Beghuin, P. van Donink, R. Ligot, J.L. Dewandel, D. Hu, D. Bates, R. Cole, R. Drummond, I.R. Thomas, C. Depiesse, E. Neefs, E. Equeter, B. Ristic, S. Berkenbosch, D. Bolsée, Y. Willame, A.C. Vandaele, S. Lesschaeve, L. De Vos, N. Van Vooren, T. Thibert, E. Mazy, J. Rodriguez-Gomez, R. Morales, G.P. Candini, M.C. Pastor-Morales, R. Sanz, B. Aparicio del Moral, J.M. Jeronimo-Zafra, J.M. Gómez-López, G. Alonso-Rodrigo, I. Pérez-Grande, J. Cubas, A.M. Gomez-Sanjuan, F. Navarro-Medina, A. BenMoussa, B. Giordanengo, S. Gissot, G. Bellucci, J.J. Lopez-Moreno, NOMAD spectrometer on the ExoMars trace gas orbiter mission: part 2—design, manufacturing, and testing of the ultraviolet and visible channel. *Appl. Opt.* **56**(10), 2771 (2017). <https://doi.org/10.1364/ao.56.002771>
- L.J. Paxton, D.E. Anderson, Far ultraviolet remote sensing of Venus and Mars, in *Venus and Mars: Atmospheres, Ionospheres, and Solar Wind Interactions*, ed. by J.G. Luhmann, M. Tatrallyay, R.O. Pepin. *Geophys. Monogr. Ser.*, vol. 66 (AGU, Washington, 1992), pp. 113–189
- J.B. Pearce, K.A. Gause, E.F. Mackey, K.K. Kelly, W.G. Fastie, C.A. Barth, The Mariner 6 and 7 ultraviolet spectrometers. *Appl. Opt.* **10**, 805 (1971)
- W.A. Podgorski, P.N. Cheimets, P. Boerner, P. Glenn, SDO-AIA mirror performance, in *Solar Physics and Space Weather Instrumentation III*, vol. 7438 (SPIE, Bellingham, 2009), p. 74380F. <https://doi.org/10.1117/12.830592>. <http://www.spiedigitallibrary.org/conference-proceedings-of-spie/7438/74380F/SDO-AIA-mirror-performance/10.1117/12.830592.short>
- R.F.L. Rice, Some practical universal noiseless coding techniques, part 2. Tech. Rep., Jet Propulsion Lab., California Inst. of Tech. (1983). <https://ntrs.nasa.gov/search.jsp?R=19830019798>
- H.A. Rowland, On concave gratings for optical purposes. *Am. J. Sci.* **s3–26**(152), 87–98 (1883). <https://doi.org/10.2475/ajs.s3-26.152.87>. <http://www.ajsonline.org/cgi/doi/10.2475/ajs.s3-26.152.87>
- N.M. Schneider, Z. Milby, S.K. Jain, F. González-Galindo, E. Royer, J.C. Gérard, A. Stiepen, J. Deighan, A.I.F. Stewart, F. Forget, F. Lefèvre, S.W. Bougher, Imaging of Martian circulation patterns and atmospheric tides through MAVEN/IUVS nightglow observations. *J. Geophys. Res. Space Phys.* **125**(8), e27318 (2020). <https://doi.org/10.1029/2019JA027318>
- V.I. Shematovich, D.V. Bisikalo, J.C. Gérard, C. Cox, S.W. Bougher, F. Leblanc, Monte Carlo model of electron transport for the calculation of Mars dayglow emissions. *J. Geophys. Res.* **113**, E02011 (2008). <https://doi.org/10.1029/2007JE002938>
- O.H.W. Siegmund, J. McPhate, T. Curtis, S. Jelinsky, J.V. Vallergera, J. Hull, J. Tedesco, Ultraviolet imaging detectors for the GOLD mission, in *Space Telescopes and Instrumentation 2016: Ultraviolet to Gamma Ray*, vol. 9905 (SPIE, Bellingham, 2016), p. 99050D. <https://doi.org/10.1117/12.2232219>. <http://www.spiedigitallibrary.org/conference-proceedings-of-spie/9905/99050D/Ultraviolet-imaging-detectors-for-the-GOLD-mission/10.1117/12.2232219.short>
- C. Simon, O. Witasse, F. Leblanc, G. Gronoff, J.L. Bertaux, Dayglow on Mars: kinetic modeling with SPICAM UV limb data. *Planet. Space Sci.* **57**, 1008–1021 (2009). <https://doi.org/10.1016/j.pss.2008.08.012>
- M.M. Sirk, E.J. Korpela, Y. Ishikawa, J. Edelstein, E.H. Wishnow, C. Smith, J. McCauley, J.B. McPhate, J. Curtis, T. Curtis, S.R. Gibson, S. Jelinsky, J.A. Lynn, M. Marckwordt, N. Miller, M. Raffantii, W. Van Shourt, A.W. Stephan, T.J. Immel, Design and performance of the ICON EUV spectrograph. *Space Sci. Rev.* **212**(1), 631–643 (2017). <https://doi.org/10.1007/s11214-017-0384-2>
- R. Souffi, S.L. Baker, J.C. Robinson, E.M. Gullikson, T.J. McCarville, M.J. Pivovarov, P. Stefan, S.P. Hau-Riege, R. Bionta, Morphology, microstructure, stress and damage properties of thin film coatings for the LCLS x-ray mirrors, in *Damage to VUV, EUV, and X-Ray Optics II*, vol. 7361 (SPIE, Bellingham, 2009), p. 73610U. <https://doi.org/10.1117/12.823836>. <http://www.spiedigitallibrary.org/conference-proceedings-of-spie/7361/73610U/Morphology-microstructure-stress-and-damage-properties-of-thin-film-coatings/10.1117/12.823836.short>
- M.H. Stevens, J.S. Evans, N.M. Schneider, A.I.F. Stewart, J. Deighan, S.K. Jain, M. Crismani, A. Stiepen, M.S. Chaffin, W.E. McClintock, G.M. Holsclaw, F. Lefèvre, D.Y. Lo, J.T. Clarke, F. Montmessin, B.M. Jakosky, N₂ in the upper atmosphere of Mars observed by IUVS on MAVEN. *Geophys. Res. Lett.* **42**, 9050–9056 (2015). <https://doi.org/10.1002/2015GL065319>
- A.I. Stewart, Mariner 6 and 7 ultraviolet spectrometer experiment: implication of CO₂⁺, CO, and O airglow. *J. Geophys. Res.* **77**, 54–68 (1972). <https://doi.org/10.1029/JA077i001p00054>

- S.W. Stone, R.V. Yelle, M. Benna, M.K. Elrod, P.R. Mahaffy, Thermal structure of the martian upper atmosphere from MAVEN NGIMS. *J. Geophys. Res.* (2018). <https://doi.org/10.1029/2018JE005559>
- S.W. Stone, R.V. Yelle, M. Benna, D.Y. Lo, M.K. Elrod, P.R. Mahaffy, Hydrogen escape from Mars is driven by seasonal and dust storm transport of water. *Science* **370**(6518), 824–831 (2020). <https://doi.org/10.1126/science.aba5229>. <https://science.sciencemag.org/content/370/6518/824>
- D.J. Strickland, J.S. Evans, L.J. Paxton, Satellite remote sensing of thermospheric O/N₂ and solar EUV. 1: theory. *J. Geophys. Res.* **100**, 12217 (1995). <https://doi.org/10.1029/95JA00574>
- D.J. Strickland, J. Bishop, J.S. Evans, T. Majeed, P.M. Shen, R.J. Cox, R. Link, R.E. Huffman, Atmospheric Ultraviolet Radiance Integrated Code (AURIC): theory, software architecture, inputs, and selected results. *J. Quant. Spectrosc. Radiat. Transf.* **62**, 689–742 (1999). [https://doi.org/10.1016/S0022-4073\(98\)00098-3](https://doi.org/10.1016/S0022-4073(98)00098-3)
- E.M.B. Thiemann, P.C. Chamberlin, F.G. Eparvier, B. Templeman, T.N. Woods, S.W. Bougher, B.M. Jakosky, The MAVEN EUVM model of solar spectral irradiance variability at Mars: algorithms and results. *J. Geophys. Res. Space Phys.* **122**(3), 2748–2767 (2017). <https://doi.org/10.1002/2016JA023512>
- M.G. Trainer, M.H. Wong, T.H. McConnochie, H.B. Franz, S.K. Atreya, P.G. Conrad, F. Lefèvre, P.R. Mahaffy, C.A. Malespin, H.L.K. Manning, J. Martín-Torres, G.M. Martínez, C.P. McKay, R. Navarro-González, Á. Vicente-Retortillo, C.R. Webster, M.P. Zorzano, Seasonal variations in atmospheric composition as measured in Gale Crater, Mars. *J. Geophys. Res., Planets* **124**(11), 3000–3024 (2019). <https://doi.org/10.1029/2019JE006175>
- M.K. Wallis, Exospheric density and escape fluxes of atomic isotopes on Venus and Mars. *Planet. Space Sci.* **26**(10), 949–953 (1978). [https://doi.org/10.1016/0032-0633\(78\)90077-6](https://doi.org/10.1016/0032-0633(78)90077-6)
- Y. Xie, A. Zhang, Y. Liu, H. Liu, T. Hu, L. Zhou, X. Cai, J. Fang, B. Yu, Y. Ge, Q. Lü, X. Sun, L. Sun, Z. Xue, Y. Xie, Y. Zheng, J. Lü, Influence of air exposure on CsI photocathodes. *Nucl. Instrum. Methods Phys. Res., Sect. A, Accel. Spectrom. Detect. Assoc. Equip.* **689**, 79–86 (2012). <https://doi.org/10.1016/j.nima.2012.06.023>. <http://www.sciencedirect.com/science/article/pii/S0168900212006729>

Publisher's Note Springer Nature remains neutral with regard to jurisdictional claims in published maps and institutional affiliations.

Authors and Affiliations

Gregory M. Holsclaw¹  · Justin Deighan¹ · Hessa Almatroushi² · Mike Chaffin¹ · John Correia³ · J. Scott Evans³ · Matthew Fillingim⁴ · Alan Hoskins¹ · Sonal K. Jain¹ · Robert Lillis⁴ · Fatma Hussain Lootah² · Jason B. McPhate⁴ · Oswald H.W. Siegmund⁴ · Regina Soufli⁵ · Kush Tyagi¹

✉ G.M. Holsclaw
holsclaw@colorado.edu

¹ Laboratory for Atmospheric and Space Physics, University of Colorado, 3665 Discovery Dr., Boulder, CO 80303, USA

² Mohammed Bin Rashid Space Centre, Dubai, UAE

³ Computational Physics Inc., Springfield, VA, USA

⁴ Space Sciences Laboratory, University of California, Berkeley, 7 Gauss Way, Berkeley, CA, 94720, USA

⁵ Lawrence Livermore National Laboratory, 7000 East Avenue, Livermore, CA 94550, USA